REVIEW ARTICLE

Epitaxial Growth in Additive Manufacturing of High-γ' Nickel-based Superalloys: Solidification Dynamics, Defect Mitigation, and Hybrid Synergy

Anhui Xiong[1,†], Xianghui Wang[1,†], Pan Ying[1,†], Chen Chang[1], Ze Li[1], Dong Zheng[1], Shuang Shi[1] and Yang Chen[1,2,*]

[1] State Key Laboratory of Advanced Casting Technologies, Nanjing University of Science and Technology, Nanjing 210094, China
[2] State Key Laboratory of light superalloys, Henan University of Science and Technology, Luoyang 471023, China

Abstract

Additive manufacturing (AM) is redefining the limits of directional solidification (DS) and single-crystal (SX) fabrication for nickel-based superalloys. By reconciling classical Bridgman theory with the extreme thermal gradients (G) and solidification velocities (V) inherent to AM, this review establishes a unified framework for controlled epitaxy. It dissects the kinetics of grain competition and the columnar-to-equiaxed transition (CET), highlighting how scan strategies and thermal management dictate melt pool geometry and the G/V ratio. A comparative assessment of laser powder bed fusion (L-PBF), electron beam powder bed fusion (EB-PBF), and directed energy deposition (DED) delineates distinct process windows for direct fabrication versus epitaxial repair. Addressing the conflict between printability and performance in high-γ' alloys, the text links defect mechanisms, specifically stray grains (SGs) driven by constitutional supercooling, complex cracking modes, and surface anomalies, to targeted mitigation strategies ranging from virtual grain selection to alloy tailoring and synergistic post-processing. Ultimately, a multi-process hybrid architecture is proposed that positions EB-PBF as the foundational platform for bulk SX formation, augmented by L-PBF or DED, to close the "manufacture–service–repair–remanufacture" engineering loop.

Keywords: additive manufacturing, superalloys, single crystal, directional solidification.

1 Introduction

Aerospace exploration and energy utilization are fundamental drivers of human progress. As critical load-bearing components in the hot sections of aero-engines and gas turbines, turbine blade

Submitted: 11 December 2025
Accepted: 11 February 2026
Published: 25 February 2026

Vol. 2, **No.** 1, 2026.
10.62762/JAMR.2025.827155

***Corresponding author:**
✉ Yang Chen
yang.chen@njust.edu.cn

† These authors contributed equally to this work

Citation
Xiong, A., Wang, X., Ying, P., Chang, C., Li, Z., Zheng, D., Shi, S., & Chen, Y. (2026). Epitaxial Growth in Additive Manufacturing of High-γ' Nickel-based Superalloys: Solidification Dynamics, Defect Mitigation, and Hybrid Synergy. *Journal of Advanced Materials Research*, 2(1), 55–85.

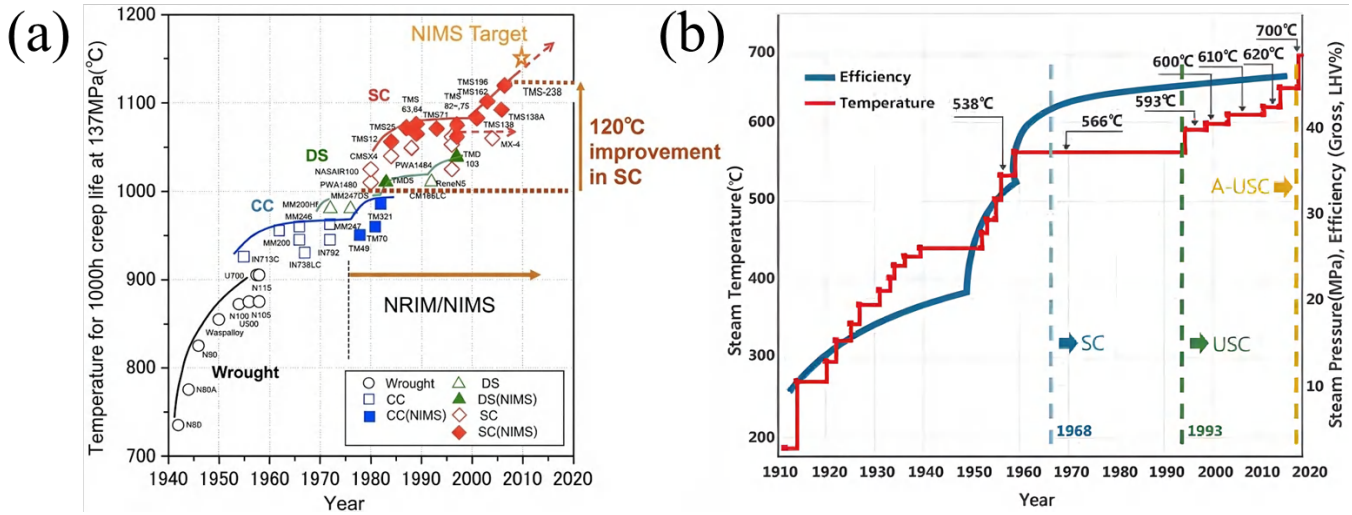

Figure 1. (a) Evolution of creep performance of Ni-base superalloys by year [2], (b) Evolution of thermal efficiency in steam power plants [3].

performance is governed not only by intrinsic high-temperature properties, such as strength, creep resistance, and oxidation resistance, but also critically by microstructural features, particularly crystallographic orientation and grain boundary morphology. Early superalloy turbine blades employed equiaxed microstructures, but grain boundaries often served as preferential sites for failure under high-temperature creep and fatigue conditions [1]. To handle higher thermal loads and improve performance, turbine blade materials have undergone a generational evolution from equiaxed to columnar-grained, and ultimately to single-crystal (SX) structures (Figure 1) [2, 3].

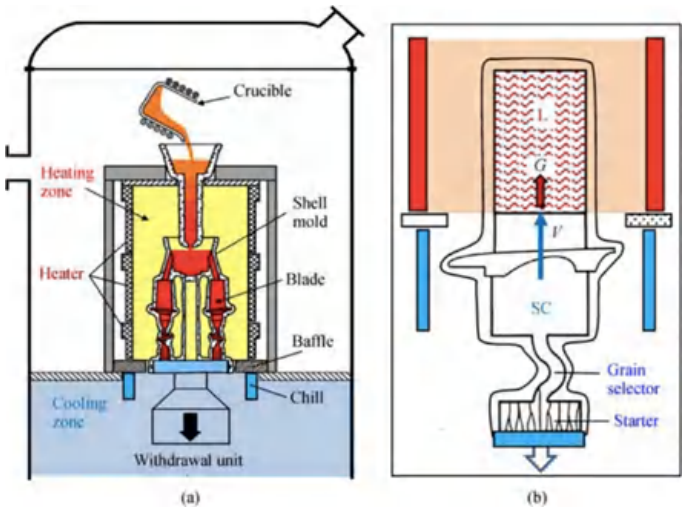

Figure 2. (a) Schematic diagram of the Bridgman furnace; (b) Grain selector for single-crystal solidification [6].

This transformation began in the late 1960s with the maturation of directional solidification (DS) technology, leading to the industrial application of DS and SX blades by manufacturers such as Pratt & Whitney. Currently, nickel-based single-crystal superalloys constitute the dominant material system for first-stage high-pressure turbine blades [4]. These components are primarily manufactured via Investment casting based on the Bridgman technique [5]. As illustrated in Figure 2, this process involves precise thermal control within a furnace, utilizing a helical grain selector to filter a single grain orientation and promote competitive growth along the heat flow direction, thereby yielding a macroscopic single crystal without grain boundaries [6]. While this route significantly enhances creep life, it suffers from a narrow processing window and high sensitivity to thermal gradients and shell stability [7].

However, this traditional manufacturing paradigm faces increasingly severe challenges. From a production standpoint, SX casting involves a time-consuming cycle that relies on sacrificial molds (Figure 3) and complex processing [8]. Casting yield is commonly limited by defects such as shrinkage porosity, inclusions, segregation, and stray grains [9, 10].

From a design perspective, the pursuit of extreme aerodynamic and thermodynamic efficiency has necessitated the integration of intricate internal cooling features, such as serpentine channels, micro-film cooling holes, and lattice structures (Figure 4) [11, 12]. Such high-aspect-ratio, thin-walled designs frequently induce ceramic core fracture or "core shift" during casting, compelling designers to compromise cooling efficiency to ensure

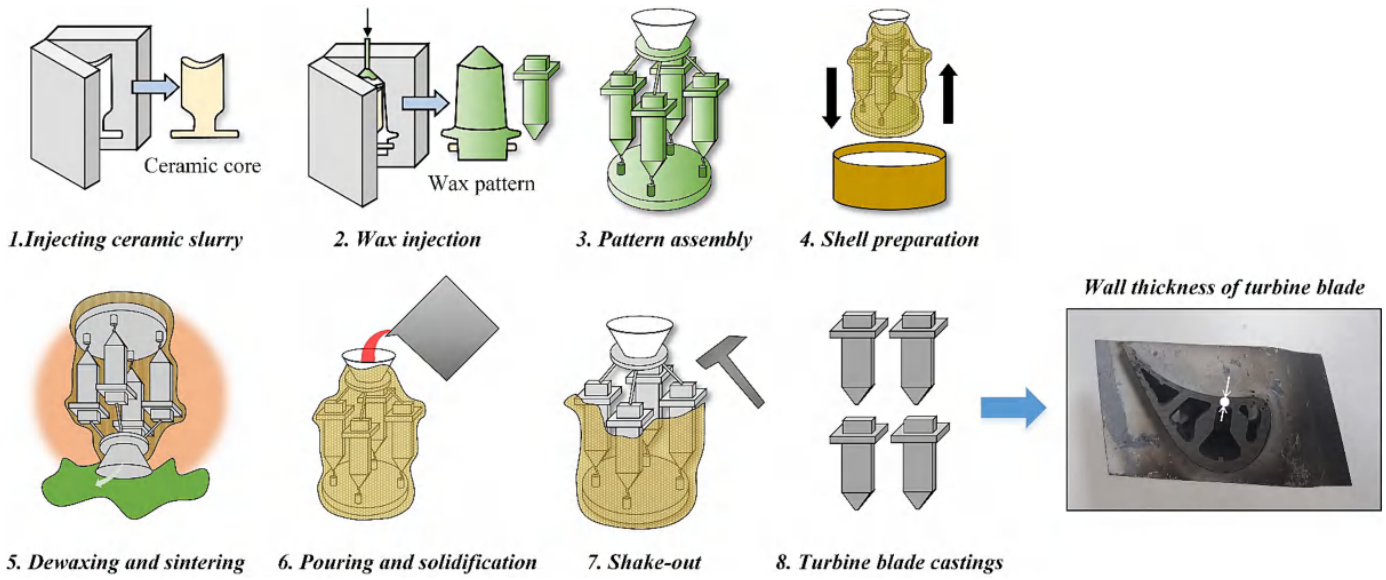

Figure 3. Workflow of the investment casting cycle for hollow turbine blade fabrication [8].

manufacturability [13]. Furthermore, given the prohibitive cost of single-crystal blades, the lack of repair techniques capable of restoring the SX metallurgy in damaged areas often results in the scrapping of entire high-value components [14].

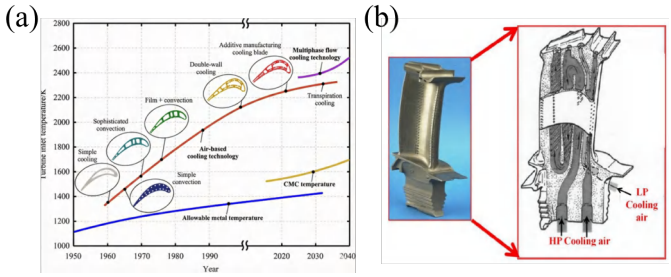

Figure 4. (a) Evolution of turbine blade cooling designs [12], (b) Trent 500 HP turbine blade [15].

Against this backdrop, Additive manufacturing (AM) offers a transformative paradigm for integrated component design, performance optimization, and repair through its layer-wise growth capability [16]. Technologies such as laser powder bed fusion (L-PBF), electron beam powder bed fusion (EB-PBF), and directed energy deposition (DED) eliminate the reliance on molds and cores, enabling the near-net-shape formation of complex internal channels while significantly improving material utilization [17–19]. Significant engineering milestones have recently been achieved in the energy and aviation sectors: L-PBF enabled Siemens Energy to reduce turbine blade development cycles from two years to two months, while EB-PBF allowed GE Aviation to mass-produce blades for the GE9X engine that are approximately 50% lighter and exhibit enhanced performance. As illustrated in Figure 5, these AM processes have successfully fabricated turbine blades with varying levels of geometric complexity [20].

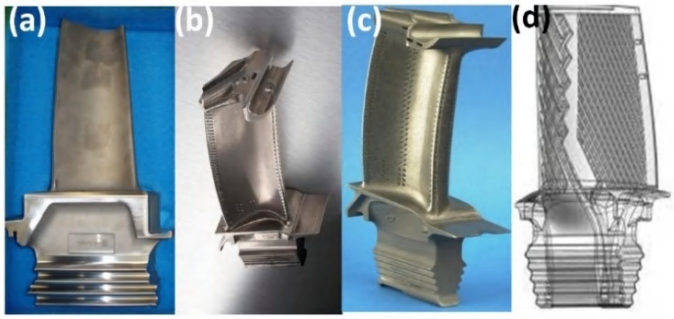

Figure 5. Turbine blades fabricated by various additive manufacturing processes [15].

Despite these successes with polycrystalline Ni-based alloys, achieving defect-free epitaxial growth of high-performance nickel-based single crystals via AM remains hindered by a fundamental metallurgical paradox: the chemical composition required for high-temperature performance is intrinsically in conflict with the rapid solidification dynamics of AM. Modern SX superalloys (e.g., CMSX-4) rely on a γ' phase volume fraction exceeding 60% to sustain service temperatures above 1000 °C, necessitating high concentrations of Al and Ti [21]. However, these elements widen the freezing range and exacerbate interdendritic segregation. In the extreme thermal cycles of AM, this solute redistribution triggers hot tearing, stray grains (SG) formation, and other defects. As shown in Figure 6, high-γ' alloys are classified as "difficult-to-weld" or "unweldable" on weldability maps due to their extreme susceptibility to

cracking [22].

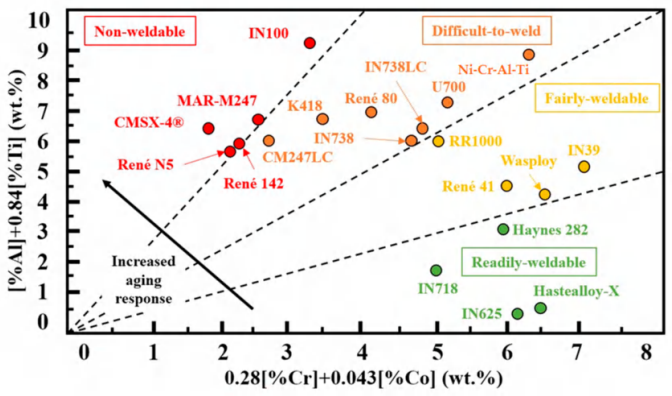

Figure 6. Weldability map of nickel-based superalloys [22].

The high thermal gradients (G) and solidification velocities (V) inherent to AM induce severe solute partitioning, leading to various cracking modes. Segregation promotes the formation of low-melting-point liquid films, which trigger solidification and liquation cracks under shrinkage stresses. Additionally, repeated thermal cycling builds up residual stress, increasing the risk of strain-age cracking during deposition or heat treatment [23]. In L-PBF, these cracks typically propagate along high-angle grain boundaries, disrupting the epitaxial structure [24–26]. Although process optimizations such as base plate preheating and multi-pass remelting have been explored, the processing window to simultaneously achieve high density and crack-free microstructures remains extremely narrow for alloys like IN738LC, with significant risks of size-dependent cracking [27–29]. Beyond cracking, the thermal history of AM disrupts the crystal structure. Strong constitutional supercooling promotes the columnar-to-equiaxed transition (CET), nucleating SGs that interrupt epitaxial growth [30, 31].

Previous reviews have addressed specific facets of this field. Basak and Das32 linked early solidification theory to epitaxial growth, while Li et al. [33] categorized the AM process systems for SX superalloys, defining the technical paths for laser repair and electron beam manufacturing. More focused studies by Liu and Shi34 examined the progress of SG suppression and numerical modeling, while Wu et al. [35] classified cracking mechanisms and alloy design strategies. However, a critical gap remains: the literature lacks a unified framework that reconciles the thermodynamic "unweldability" of high-γ' alloys with the divergent kinetic requirements across different AM platforms. The trade-off between epitaxial continuity and defect mitigation remains a persistent bottleneck in process selection.

This review establishes a unified framework based on thermal G and V to align metallurgical constraints with the distinct thermal histories of L-PBF, DED, and EB-PBF. L-PBF operates at high G and V magnitudes, enabling precise microstructural control but increasing susceptibility to strain-age and solidification cracking due to extreme thermal transients [36]. DED offers multi-axis flexibility for localized repair, yet the difficulty in maintaining stable G and V values over large volumes often leads to solute segregation and loss of epitaxial continuity. In contrast, EB-PBF utilizes high-temperature preheating to reduce thermal stress and suppress γ' precipitation, enabling the crack-free fabrication of 'unweldable' alloys, although it typically exhibits higher surface roughness compared to L-PBF [37–39].

By synthesizing insights across these platforms, this work addresses the fundamental scientific challenges in the AM of high-γ' nickel-based superalloys. The review systematically examines the solidification dynamics governing epitaxial growth, analyzes the mechanisms for defect mitigation regarding cracking and stray grains, and explores the potential of synergistic hybrid strategies to provide a technical roadmap for next-generation, high-performance hot-section components.

2 Fundamentals of controlled solidification in AM

To understand grain control in AM, it is essential to contrast it with conventional SX growth. Conventional SX fabrication relies on the Bridgman method, where a ceramic mold containing molten alloy is withdrawn at a constant speed through a stable temperature gradient. This process typically maintains a thermal gradient G of $1 \times 10^3\,\mathrm{K\,m^{-1}} to 1 \times 10^4\,\mathrm{K\,m^{-1}}$ at the solid/liquid interface [40], creating quasi-equilibrium conditions that yield uniform columnar dendrites aligned with the withdrawal axis. However, AM operates under rapid, non-equilibrium solidification. High-energy beams generate microscopic melt pools within milliseconds [41], producing G values of $1 \times 10^5\,\mathrm{K\,m^{-1}} to 1 \times 10^7\,\mathrm{K\,m^{-1}}$ and cooling rates up to $1 \times 10^5\,\mathrm{K\,s^{-1}}$, far surpassing the $0.5\,\mathrm{K\,s^{-1}} to 10\,\mathrm{K\,s^{-1}}$ typical of casting [42].

The G–V framework serves as the unifying descriptor for these different processes, where the ratio G/V

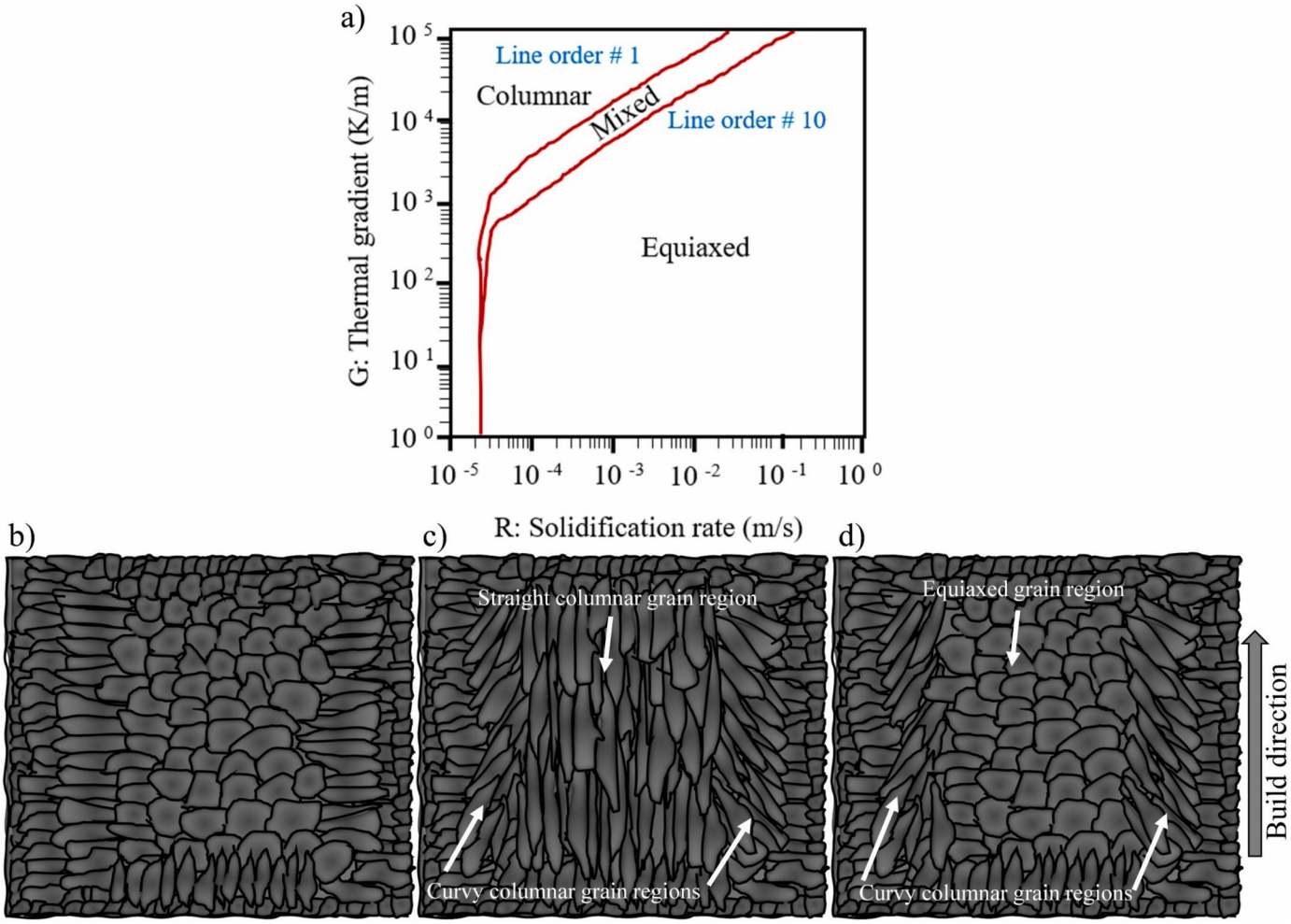

Figure 7. Effect of Scanning Strategy on the CET in AM [43].

dictates the morphology and the product $G \times V$ defines the scale of the microstructure. As shown in Figure 7, the G/V ratio determines grain morphology, which ranges from planar to equiaxed structures. Adjusting settings such as laser power, scan speed, and scan strategy allows researchers to tailor the microstructure from random grains to precise directionally solidified (DS) architectures [44].

Unlike the steady-state Bridgman method, AM solidification is transient and multidirectional, forcing the growth front through a rapidly shifting trajectory in the G–V plane. Thermal fluctuations and complex melt convection in this environment often trigger stray grains and orientation failure. Because the solidification path evolves so quickly, achieving stable epitaxial growth, where grains extend continuously in a single direction, requires precise management of these thermal perturbations within the G–V map.

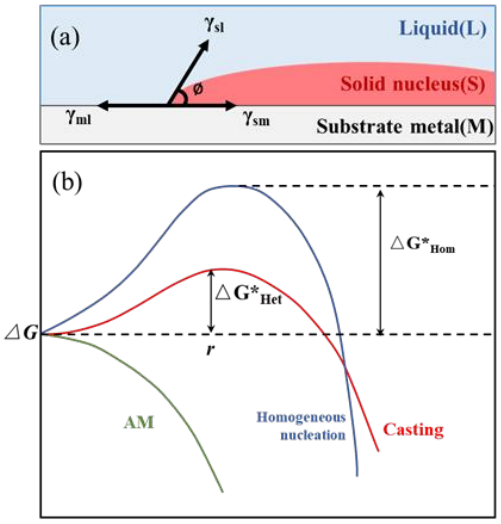

Figure 8. (a) Contact interface between the solid nucleus and the substrate/liquid phase; (b) Gibbs free energy evolution for homogeneous nucleation in casting/AM.

2.1 Thermodynamics of Epitaxial Growth

While epitaxial solidification is often described in terms of heterogeneous nucleation, this classification is strictly a thermodynamic analogy used to rationalize the near-vanishing energy barrier rather than a description of discrete nucleation events. In AM,

true epitaxy proceeds via continuous lattice extension from the remelted substrate into the melt pool. In the near-zero misorientation limit, the solid–solid interfacial energy (γ_{SM}) effectively vanishes, driving the contact angle (θ) $\rightarrow 0°$. Thermodynamic equilibrium at the triple junction comprising the solid nucleus (S), substrate (M), and liquid (L) is dictated by Young's equation, as illustrated in Figure 8(a) [43]:

$$\gamma_{ML} = \gamma_{SM} + \gamma_{SL}\cos(\theta) \tag{1}$$

where:

- γ_{SM}: solid nucleus–substrate interfacial energy,
- γ_{ML}: substrate–liquid interfacial energy,
- γ_{SL}: solid nucleus–liquid interfacial energy,
- θ: contact angle (wetting angle).

In conventional casting, heterogeneous nucleation typically occurs on inclusions or oxide particles that differ significantly in composition and crystal structure from the matrix. In such cases, both γ_{SM} and γ_{SL} are substantial, resulting in a large contact angle and requiring significant undercooling to overcome the nucleation barrier.

By contrast, in AM under epitaxial solidification conditions, the newly formed solid and the underlying substrate are nearly identical in chemical composition and crystal structure. When the misorientation angle is small, the solid–solid interface becomes a low-energy boundary, satisfying:

$$\gamma_{SM} \ll \gamma_{ML} \approx \gamma_{SL} \tag{2}$$

This implies $\theta \rightarrow 0°$, corresponding to near-complete wetting. Consequently, the nascent nucleus favors lateral spreading along the substrate rather than forming an isolated sphere particle suspended in the melt. This constitutes the thermodynamic foundation for epitaxial growth in AM.

From an energetic perspective, the formation of a solid phase is governed by the Gibbs free energy change (ΔG_{het}), which balances the volumetric free energy reduction ($V_s \Delta G_V$) against the cost of creating a new S-L interface ($A_S \gamma_{SL}$):

$$\Delta G_{het} = -V_s \Delta G_V + A_S \gamma_{SL} \tag{3}$$

The critical energy barrier (ΔG^*_{het}) is scaled by the geometric shape factor $S(\theta)$:

$$\Delta G^*_{het} = \left(\frac{16\pi}{3}\frac{\gamma_{SL}^3}{\Delta G_V^3}\right) S(\theta) \tag{4}$$

where $S(\theta)$ is defined as:

$$S(\theta) = \frac{[2+\cos(\theta)][1-\cos(\theta)]^2}{4} \tag{5}$$

In AM processes such as DED or PBF, this relationship provides the thermodynamic rationale for epitaxial solidification. When the melt pool sufficiently remelts the underlying layer, the liquid metal interfaces with a crystalline template of the same orientation. This creates a state of near-perfect wetting where the misorientation angle and the resulting contact angle θ approach zero. As $S(\theta) \rightarrow 0$, the thermodynamic barrier ΔG^*_{het} effectively vanishes as shown in Figure 8(b). This explains why the solid phase almost invariably grows as a continuous extension of the substrate orientation instead of forming random equiaxed nuclei. In this regime, the stability of the solidification front is no longer limited by nucleation kinetics but is instead controlled by dynamic factors such as solidification velocity, thermal gradients, and solute transport [32, 45, 46].

2.2 Kinetics and Grain Selection Mechanisms

While thermodynamics favors epitaxial solidification, the actual microstructural selection in AM is ultimately governed by solidification kinetics, specifically G and V [47]. Classical theory maps these outcomes onto $G-V$ diagram, defining the "solidification microstructure selection map" [48]. Assuming one-dimensional heat flow, the cooling rate can be approximated as:

$$\dot{T} \approx G \cdot V \tag{6}$$

In this framework, G controls interface stability while V determines the kinetic progress of the solidification front. To suppress CET, DS theory imposes the Hunt criterion [34]:

$$\frac{G^n}{V} > K_{CET} \tag{7}$$

where K_{CET} accounts for alloy composition, nucleation density, and convection [49, 50]. In essence, maintaining a sufficiently high G/V ensures the columnar front outpaces premature equiaxed nucleation. A high G/V ratio suppresses constitutional supercooling, stabilizing columnar

epitaxy. Conversely, a low G/V ratio generates a wide undercooled region ahead of the solidification front, enabling heterogeneous nucleation of stray grains and initiating the CET [51]. As illustrated in Figure 9, decreasing G/V shifts the morphology from planar to cellular, then to columnar dendritic, and finally to equiaxed structures [52].

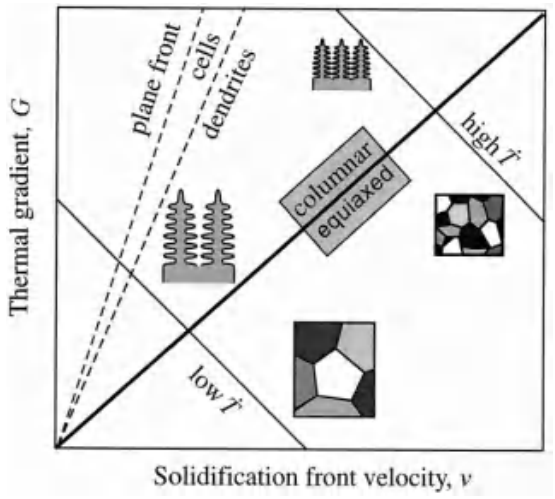

Figure 9. Regulation of growth morphologies [52].

Applying these principles to AM requires a clear distinction between the fundamental solidification physics inherited from casting and the unique characteristics introduced by the additive process. While AM shares core drivers with traditional theory, such as constitutional supercooling and dendrite fragmentation, the high-energy melt pool environment introduces variables that fundamentally alter grain selection. Partially melted powder particles at the pool periphery act as effective heterogeneous nucleation sites, capable of triggering equiaxed grain formation even under high thermal gradients. This is compounded by intense Marangoni convection and rapid fluctuations in the G and V vectors actively transport these nuclei into the undercooled zone. This promotes mechanical blocking, where a dense equiaxed network geometrically obstructs the columnar front once the equiaxed volume fraction ϕ_c exceeds a critical threshold ($\phi_c = 0.49 - 0.66$) [50, 51, 53]. In AM, fluid flow directly influences this blocking probability [54, 55]. Additionally, the cyclic thermal loading unique to AM can drive solid-state recrystallization, creating misoriented nuclei not typically considered in primary solidification theory.

However, AM further complicates this framework because G and V values far exceed those in casting and fluctuate rapidly due to transient melt pool dynamics, causing solidification paths to traverse multiple microstructural regimes within a single component [56]. Consequently, Hunt-type criteria serve as qualitative guidelines rather than strict boundaries. High nucleation densities, stemming from unmelted powder or dendrite fragmentation, can induce equiaxed growth even under steep thermal gradients. Managing melt pool stability to limit these nucleation sources is therefore critical for suppressing stray grains in DED and L-PBF [57].

Building on this concept, Gäumann et al. [58] adapted the Hunt model for laser DED of CMSX-4, defining a "safe zone" for SX repair by mapping process parameters onto the G–V plane for the alloy. Experimental results confirm that specific processing routes can successfully maintain single-orientation columnar structures.

Even within the stable G/V regime, epitaxy is rarely perfect over long build heights. Complex scan paths continuously shift the thermal gradient vector, causing dendrites to deflect. Over multiple layers, this accumulates into macroscopic crystal orientation bending [59]. Furthermore, cyclic thermal stresses drive plastic deformation and lattice rotation, manifesting as orientation gradients in Electron Backscatter Diffraction (EBSD) maps. Severe heat buildup can also trigger recrystallization, generating misoriented nuclei that create high-angle grain boundaries and potential crack initiation sites [30, 31, 60, 61]. Recent evidence suggests this evolution results from coupled thermal-flow guidance and stress-induced rotation, offering a potential route for programmable crystallographic control [57, 62].

3 Additive Manufacturing Platforms

In AM of high-γ' superalloys, precise control over grain architecture is essential to suppress hot cracking and ensure high-temperature performance. Microstructures are therefore classified within a rigorous crystallographic framework. SX material is defined by the complete absence of high-angle grain boundaries. DS columnar structures consist of multiple grains that share a common crystallographic texture but are separated by high-angle grain boundaries. Between these extremes lies the quasi-SX material, which refers to low-misorientation polycrystals with grain boundary misorientations typically in the range of 5° to 10° [63].

Although epitaxial growth and the CET in AM are often compared to Bridgman directional solidification, this analogy is fundamentally incomplete. AM melt

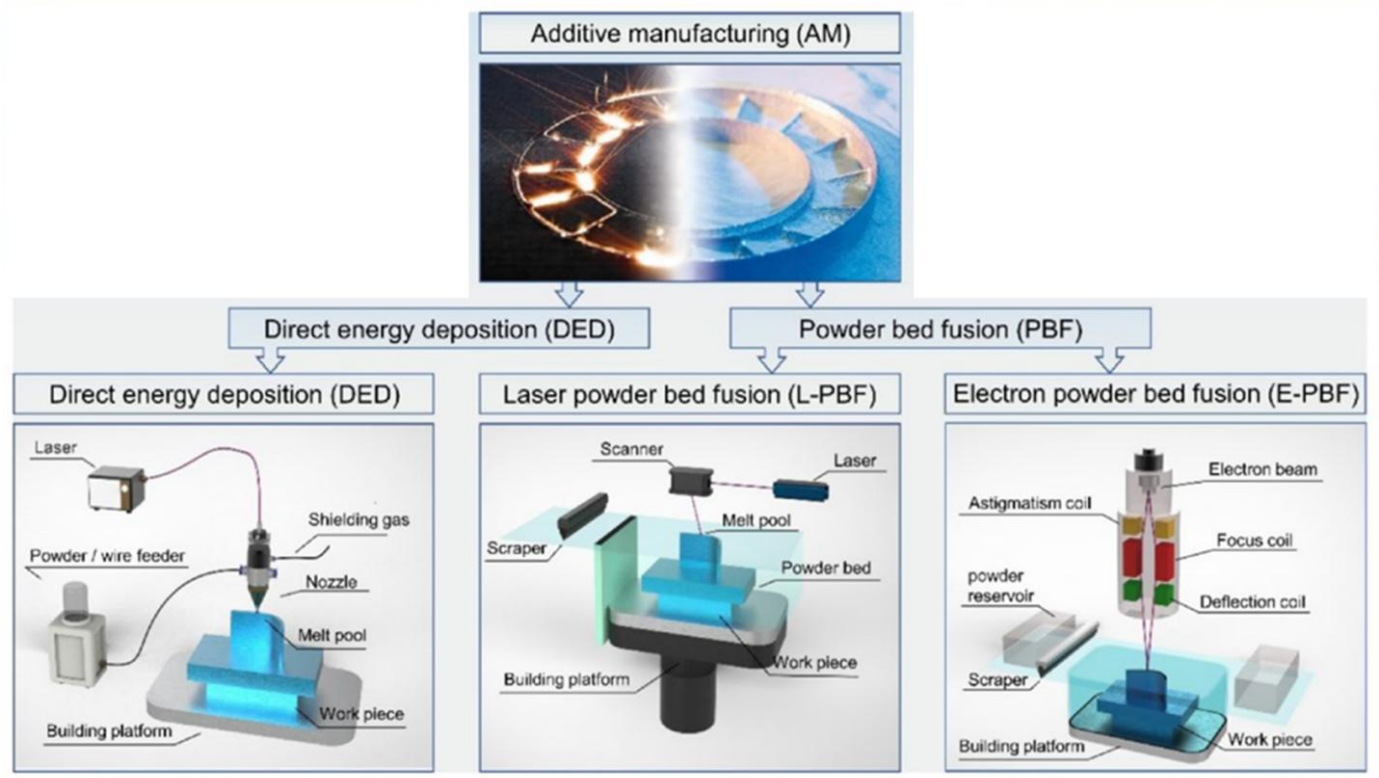

Figure 10. Classification of metal AM processes [64].

pools are highly transient, with G and V fluctuating rapidly in both magnitude and direction. These dynamic conditions produce highly localized and time-varying G/V ratios, which critically govern defect formation in weld-sensitive high-γ' superalloys. Furthermore, repeated remelting and layer-wise reheating subject the material to intense thermal cycling. This can induce recrystallization and grain boundary migration, phenomena that are notably absent under the steady-state conditions of conventional Bridgman processing.

As classified in Figure 10, the primary platforms, including L-PBF, EB-PBF and DED, offer complementary capabilities [64]. These processes differ in their ability to balance fine feature resolution, thermal stress control, and resistance to solidification cracking in difficult-to-weld alloys. This intrinsic complementarity provides the foundation for the hybrid synergy strategies discussed in the following sections.

3.1 Laser powder bed fusion

L-PBF is an AM technique that selectively melts fine metallic powder spread on a substrate using a focused laser beam under an inert atmosphere [65]. The process builds components layer-wise, characterized by extremely high cooling rates and steep thermal gradients. These solidification dynamics promote preferential columnar grain growth along the direction, often resulting in pronounced crystallographic textures or "quasi-SX" microstructures. However, this rapid solidification concurrently induces high residual stresses and increases susceptibility to hot cracking, particularly in high-γ' superalloys.

For weldable alloys such as IN718, L-PBF demonstrates significant capability in tailoring texture and grain morphology. Gokcekaya et al. [66] utilized bidirectional scanning to create distinct architectures, including a quasi-SX structure (referred to as single crystal mimetic) with near ⟨110⟩ orientation, a crystallographically layered microstructure (CLM), and a weakly textured polycrystalline microstructure (Figure 11). Mechanical testing indicated that the CLM architecture enhanced ductility while maintaining high yield strength, offering a viable compromise between process feasibility and performance when SX is unattainable. This strategy highlights the potential for site specific microstructural control in AM to achieve targeted mechanical properties without the requirement for perfect crystallographic continuity.

Experiments on SX substrates further highlight both the potential and limitations of L-PBF. Yang et al. [36] successfully fabricated a 2-mm-tall

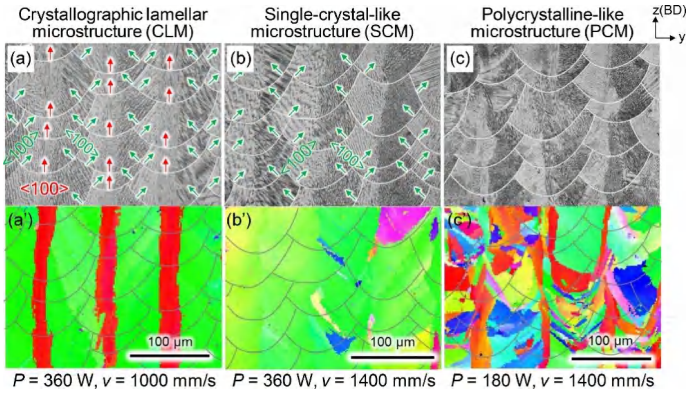

Figure 11. SEM images and IPF maps of different crystal structures in AM nickel-based superalloys [66].

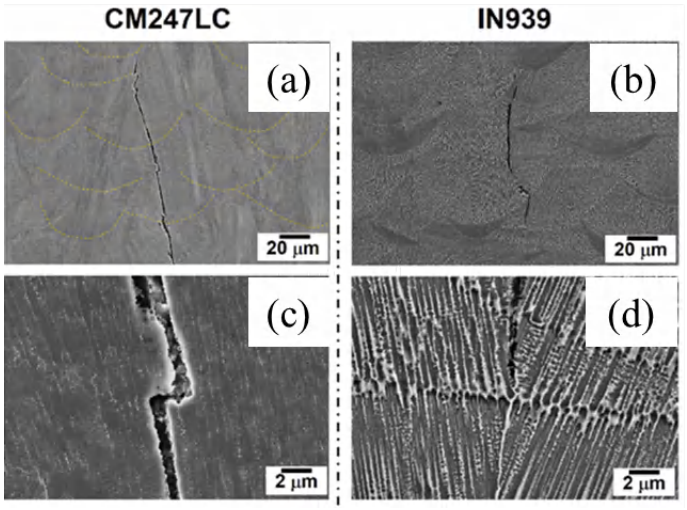

Figure 12. SEM images of CM247LC and IN939 alloys produced by L-PBF [71].

directionally solidified structure on an SX SRR99 baseplate, confirming the potential for epitaxial growth. However, increasing the deposit height to 6 mm introduced significant orientation deviation and internal cracking, revealing that long-range epitaxial stability is severely constrained by the high cooling rates and residual stresses inherent to the process. Similarly, repair studies on CMSX-4 substrates show that while localized epitaxial deposition is feasible, the process window narrows rapidly with increasing build volume [67, 68].

High-γ' superalloys, such as CM247LC and IN738LC, face particularly severe challenges with hot cracking and strain-age cracking in L-PBF. These alloys are prone to solidification, liquation, and strain-age cracks that propagate along high-angle grain boundaries, driven by segregation and evolving residual stresses [37, 69, 70]. Even with optimized parameters and post-processing, complete crack elimination in alloys like CM247LC remains difficult, with only partial reductions in crack density typically achievable (Figure 12) [71].

Recent efforts have focused on expanding L-PBF capabilities through alloy design and process innovation. Modifications such as reducing Hf and Al content have moderately lowered crack sensitivity in CM247LC and IN738LC [37, 69, 70]. Concurrently, integrated workflows combining Hot Isostatic Pressing (HIP) and tailored heat treatments have improved the consistency of repaired zones on SX substrates [68, 72].

Compared to "making whole new blades", the most realistic breakthrough for AM in high-temperature Ni-based SX components remains the epitaxial repair of high-value-added blades. Centering on this demand, Scanning Laser Epitaxy proposed by Acharya et al. [67] through a multi-physics model coupling heat-fluid-solidification, systematically simulated the temperature field, melt pool flow, dendrite growth, and segregation behavior of single-crystal alloys like CMSX-4 and IN100 under local remelting conditions. They established a quantitative correlation among process parameters, melt pool morphology, dendrite spacing, and epitaxial continuity, and experimentally verified that a crack-free, orientation-consistent epitaxial layer could be achieved through single-pass or even few-pass scanning. These works provided an important theoretical basis for the window construction of subsequent L-PBF repair processes.

Recently, repair cases for actual engineering damaged blades have also gradually increased. Wang et al. [72] used CM247LC powder to repair the blade tip and local damage areas of cast SRR99 single-crystal blades via L-PBF. After HIP and subsequent heat treatment, the CM247LC/SRR99 interface achieved crack-free metallurgical bonding, the γ/γ' structure in the repair zone was close to the matrix, tensile strength reached 791 MPa, and fracture occurred on the SRR99 base material side, proving the reliability of the repair joint.

While L-PBF has historically been constrained by the high cracking susceptibility of high-γ' superalloys, emerging mitigation strategies are extending its applicability beyond simple component repair. High-temperature preheating has proven effective in suppressing hot cracking in alloys such as CM247LC and IN713LC by reducing thermal gradients and lowering cooling rates [73]. Innovations in scan strategy design, such as the progressive remelting technique applied to Mar-M247,

further inhibit defect formation by optimizing the transient temperature field and managing residual stresses [74]. Complementary to these process-level controls, alloy tailoring addresses crack sensitivity at the metallurgical level, as demonstrated by the development of weldable compositions like LW 4275 [75].

3.2 Electron beam powder bed fusion

EB-PBF is defined by its utilization of a high-energy electron beam within a high-vacuum environment [76]. A distinguishing feature is the ability to preheat the entire powder bed to 900–1100 °C. This maintains elevated component temperatures throughout fabrication, significantly lowering thermal gradients and cooling rates to mitigate thermal stress and hot cracking. Additionally, electromagnetic scanning enables inertia-free beam deflection, offering superior flexibility in tailoring the thermal field and the G/V ratio [77–79].

In 2016, Ramsperger et al. [63] demonstrated the feasibility of directly fabricating SX structures from CMSX-4 powder via EB-PBF without using seed crystals or physical selectors. By optimizing scan strategies and energy input, they achieved a transition from polycrystalline to SX structures spanning 15 mm in width. This indicates that high preheating combined with moderate cooling facilitates SX nucleation and growth through a "virtual grain selection" mechanism.

This approach has since been successfully extended to other high-γ' superalloys, including IN738LC, yielding crack-free epitaxial specimens [80–82].

Precise thermal management is critical for processing non-weldable alloys. In studies on IN738LC, Li et al. [28] maintained the powder bed at approximately 1000 °C using multi-stage preheating, effectively suppressing both liquation and strain-age cracking. As illustrated in Figure 13, this multiple preheating process reduces thermal gradients and residual stresses, transitioning susceptible high-angle grain boundaries into crack-resistant low-angle grain boundaries despite the presence of low-melting phases such as γ/γ' eutectics.

Columnar growth in EB-PBF is fundamentally governed by both the G/V ratio and anisotropic residual stress fields. As shown in Figure 14, a persistent melt pool is a prerequisite for SX growth; high area energy density ensures melt pool continuity, which suppresses stray grain nucleation and facilitates uniform epitaxial growth [83]. Building

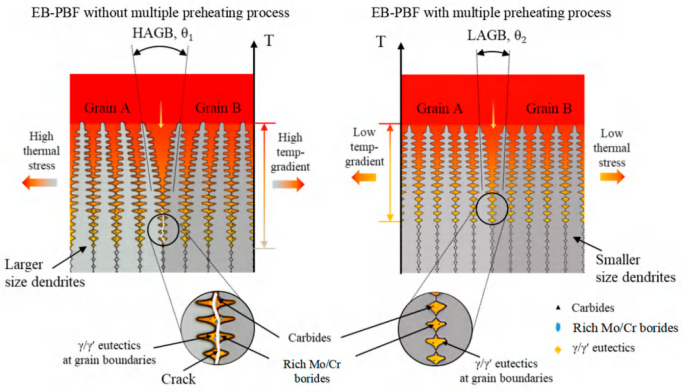

Figure 13. Mechanism of liquation cracking in AM nickel-based superalloys [28].

on this thermal stability, specialized scan strategies such as the μ-Helix utilize coupled thermal and stress fields to drive the progressive alignment and coalescence of favorably oriented dendrites. This mechanism effectively functions as a "virtual grain selector" that eliminates misoriented grains without the need for physical selection geometry [84]. Furthermore, specific hatching strategies can induce controlled "crystallographic twisting", allowing for the programmable rotation of secondary dendrite orientations along the build height. This capability offers new avenues for optimizing microstructures in complex geometries like twisted blades [85].

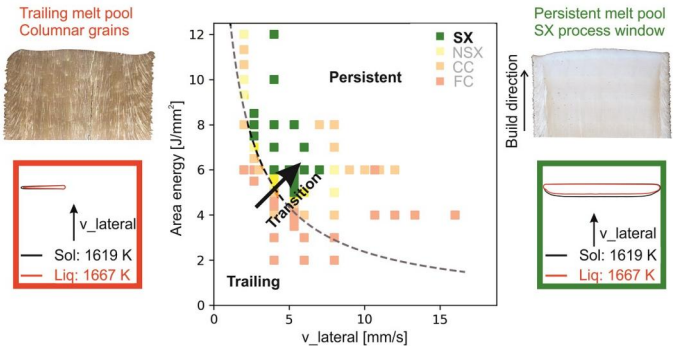

Figure 14. SX process window for EB-PBF of CMSX-4 alloy [83].

Mechanically, DS components fabricated by EB-PBF exhibit tensile and creep properties comparable or superior to conventionally cast materials after HIP and heat treatment. As shown in Figure 15, EBM-processed microstructures maintain a consistent strength advantage over cast counterparts at elevated temperatures. These samples also exhibit a pronounced increase in elongation, which mitigates the risk of brittle fracture during high-temperature deformation [79]. Specifically, crack-free Mar-M247

samples produced with controlled melt pool geometries demonstrate performance on par with cast counterparts while avoiding the recrystallization issues common in L-PBF. However, the high thermal background may lead to γ' coarsening, a factor that requires further investigation regarding its impact on high-temperature ductility [86].

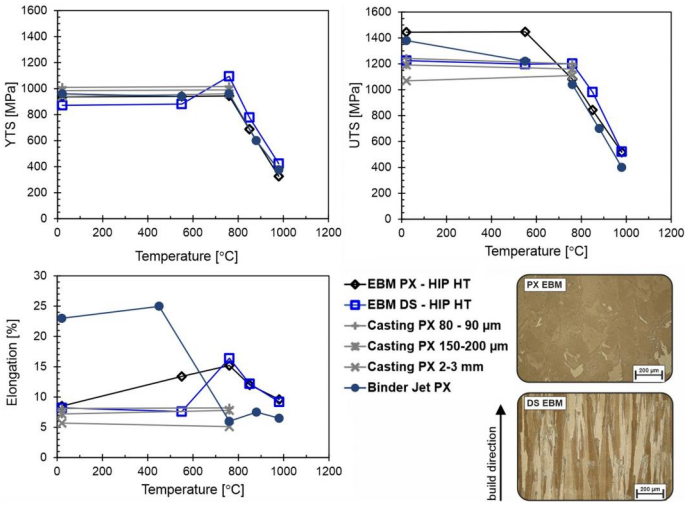

Figure 15. Tensile properties of HIP-treated and heat-treated EBM M247 compared with cast CM247LC [79].

Despite its advantages, EB-PBF faces practical limitations that necessitate synergistic hybrid strategies. The electron beam spot size restricts resolution, making it less capable than L-PBF for fabricating fine internal cooling channels. Moreover, high-temperature preheating causes powder sintering, which complicates the removal of residual material from intricate cavities. The stringent requirements for vacuum and temperature control also impose significant equipment demands. Nevertheless, EB-PBF currently remains the most promising platform for the direct AM of high-γ' SX superalloys.

3.3 Directed energy deposition

Unlike powder bed systems, DED utilizes a focused heat source to generate a melt pool with simultaneous coaxial or lateral feedstock delivery. This configuration fundamentally governs the solidification dynamics: DED typically operates with lower cooling rates and larger molten volumes compared to PBF, enabling significantly higher deposition rates and build scalability. These characteristics make it uniquely suited for epitaxial repair of in-service SX components by enabling crystallographically aligned growth and a robust metallurgical bond, embodying the synergy between traditional casting and additive restoration [87, 88].

The primary challenge in DED of high-γ' superalloys lies in maintaining epitaxial continuity while mitigating defects such as stray grains and hot cracking [89–91]. In engineering practice, Gäumann et al. [58] established a viable process window for CMSX-4 blade repair in 2001, successfully demonstrating multi-layer epitaxial deposition on damaged blade platforms. This work laid the methodological groundwork for SX control in laser-based additive repair. Subsequently, As summarized by Vilar and Almeida [91] in their review, extensive DED repair trials on CMSX-4 and Rene N5 blades have demonstrated that low-misorientation epitaxial growth can be maintained over heights of tens of millimeters when the thermal field and substrate remelting depth are tightly controlled.

To strictly control the transition from epitaxial growth to misoriented grains, a critical defect mode in epitaxial deposition, recent research has focused on precise manipulation of melt pool morphology. Zhang et al. [92] demonstrated that dendrite orientation is governed by the geometric aspect ratios of the melt pool. They identified the depth-to-height ratio (d/h) as a decisive parameter: a dual-orientation structure prevails when $d/h < 0.48$, whereas exceeding this threshold triggers a triple-orientation growth competition. By engineering shallow, elongated melt pools through reduced heat and mass input, the competitive growth of unfavorable orientations is suppressed without compromising interfacial integrity. These fundamental solidification principles have been successfully translated into industrial applications, with DED-based repair now well-validated; for instance, IN718 blade tip repairs are systematically evaluated via hardness and wear resistance across varying process parameters [93].

Advanced numerical simulation has become indispensable for predicting solidification dynamics in DED. Bhure et al. [94] developed a numerical framework coupling thermal, fluid, and phase-change physics to predict dendrite arm spacing and columnar-to-equiaxed transitions in alloys such as IN718. Their simulations showed excellent agreement with experimental EBSD observations of solidification morphology and microstructure. This model-driven approach has since been extended to DED of SX alloys like CMSX-4, enabling in silico optimization of process parameters for DS and the subsequent experimental realization of quasi-SX rods, significantly reducing

trial-and-error costs.

Notably, DED is evolving beyond repair toward the direct fabrication of large-scale quasi-SX structures. Recent DED studies show that moderate substrate preheating, optimized powder feed angles, and tailored scan strategies can yield highly anisotropic columnar or quasi-SX microstructures in CMSX-4, with continuous columnar heights reaching tens of millimeters, highlighting its emerging potential for bulk SX component manufacturing [95].

Industrially, DED validates the hybrid synergy paradigm by extending the lifecycle of cast components. Manufacturers such as Rolls-Royce and Pratt & Whitney have implemented DED for the geometric restoration of high-stress areas, including compressor blade flanges and turbine disk seals [96]. Figure 16 shows the actual turbine blade after DED repair [97].

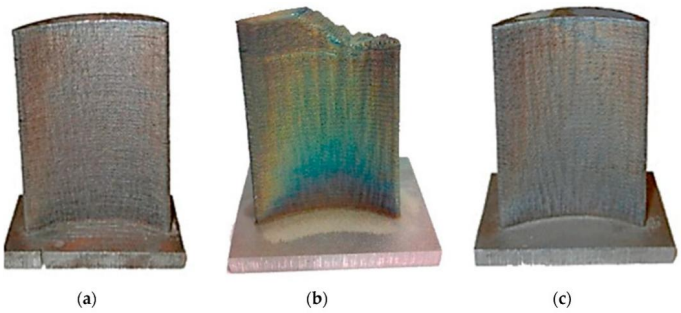

Figure 16. (a) Turbine blade produced via DED; (b) Damaged turbine blade; (c) Blade repaired using DED [97].

However, extending this technology from local repair to "certifiable, full-size SX fabrication" faces distinct bottlenecks. In summary, while DED offers distinct advantages for SX epitaxial repair and large-volume quasi-SX fabrication due to its tunable heat input and engineerable melt pool geometry, its relatively large melt pools and lower cooling rates increase susceptibility to hot tearing, stray grain formation, and coarse primary phases in high-γ' superalloys. Furthermore, the resulting surface roughness and limited resolution render it unsuitable for directly fabricating intricate features like micro-cooling channels. Additionally, challenges remain in ensuring orientation matching in high-stress regions such as blade roots. Consequently, these limitations often necessitate hybrid integration with machining or complementary AM processes.

3.4 Process comparison

The three AM processes fulfill distinct yet complementary roles within the DS and SX manufacturing chain, governed by their unique thermal histories. L-PBF achieves the highest G and cooling rates, promoting pronounced columnar growth. In L-PBF of M247, the localized heat input results in an extreme G of up to 10^7 K/m [78]. However, the extreme G and V induce significant residual stresses, increasing susceptibility to strain-age cracking in high-γ' superalloys. While its superior resolution is ideal for complex features like internal cooling channels, the high cooling rate limits its application in crack-sensitive "non-weldable" alloys.

In contrast, EB-PBF leverages high-temperature preheating (> 1000°C) to maintain a low G and thermally stabilized environment. For M247, the preheated state moderates the localized heat input, resulting in a significantly lower G of approximately 10^4 to 10^5 K/m [78]. This effectively suppresses residual stresses and hot tearing, enabling the direct fabrication of SX components from high-γ' superalloys like CMSX-4. Yet, this sustained thermal exposure increases the risk of recrystallization and γ' coarsening during the build.

DED occupies an intermediate position, characterized by lower G/V ratios and millimeter-scale melt pools. This thermal profile makes it particularly susceptible to stray grain formation via the CET and liquation cracking within its extensive large Heat Affected Zone (HAZ). While its resolution necessitates post-machining, it excels in epitaxial repair and large-volume deposition.

These distinct thermal regimes give rise to process-specific defect mechanisms, intrinsically linked to each platform's "thermal window." L-PBF is dominated by strain-age cracking due to rapid thermal cycling and high stress. EB-PBF operates within a "safety window" for cracking but is limited by the recrystallization threshold. DED's primary challenge is maintaining crystallographic continuity (avoiding stray grains) and preventing liquation cracking caused by its high heat input and broad HAZ. The key distinctions between L-PBF, EB-PBF, and DED are systematically compared in Table 1.

Future advancements will likely rely on multi-technology synergy rather than a single dominant process. A robust manufacturing architecture for complex SX components might employ EB-PBF to fabricate the monolithic SX

substrate, ensuring crystallographic continuity. Subsequently, L-PBF can construct high-resolution features like cooling ribs, while DED handles service-induced repairs. This integrated approach effectively establishes a closed loop of "Manufacture–Service–Remanufacture".

4 Solidification Dynamics and Crystallographic Control

In AM, macroscopic structures typically feature columnar grains growing epitaxially along the build direction. At the microscopic scale, however, dendrite morphology, orientation, and texture intensity are strictly governed by local heat flow and solidification dynamics. While G and V are the fundamental physical parameters governing DS and the CET, they are not directly controllable. Instead, they must be indirectly modulated through process parameters such as scan strategy, thermal management, and energy input [105, 106].

It is important to clarify that "crystallographic control" in AM is probabilistic and statistical rather than deterministic. Unlike traditional casting with physical molds, AM relies on competitive growth and suppression mechanisms where grains with the most favorable crystallographic orientation relative to the local heat flow outcompete misaligned neighbors. The differing degrees of tunability offered by various AM processes in regulating these variables ultimately determine their suitability for DS and SX applications.

4.1 Thermal Field Engineering via Scan Strategy Optimization

Scan strategies function as the primary lever for microstructural control by dictating the heat source trajectory. This process directly shapes melt pool morphology and transient heat flow direction. Unlike conventional DS, which relies on physical grain selectors (e.g., spiral selectors), AM utilizes the spatiotemporal modulation of thermal fields to generate a continuously moving "virtual grain selector" at the solidification front [77, 107].

The efficacy of this "virtual selector" varies significantly across AM modalities: in L-PBF, it is weak and highly local, as the small melt pool and rapid cooling cycles often reset the grain selection process with each new layer; in EB-PBF, it is persistent and cumulative, owing to the high-temperature powder bed and vacuum environment, which enable continuous grain selection and evolution over many layers; and in DED, it is strongly governed by geometry and melt

Table 1. Comparative Analysis of AM Technologies for Directional/Single-Crystal Fabrication.

Feature	L-PBF	EB-PBF	DED
Heat Source	Laser	Electron Beam	Laser
Environment	Inert Gas (Ar, N_2)	High Vacuum	Inert Gas Shielding
Substrate Preheat	Optional, usually 200°C	Required, 1000°C	Optional, usually low
Cooling Rate	10^5–10^7 K/s	10^4–10^6 K/s	10^2–10^3 K/s
Thermal Gradient	10^6–10^7 K/m	10^5–10^6 K/m	10^3–10^4 K/m
Surface Roughness	Low	Medium	High
Build/Deposition Rate	Low	Medium	High
Primary Defects Mode	Hot/Strain-age cracking; keyhole porosity; gas porosity	Recrystallization; γ' coarsening; Shrinkage porosity	Stray grains; Warpage; Lack of fusion; Liquation cracking; porosity
Melt Pool Geometry	Sub-millimeter; "Fish-scale"	Broad and shallow; Controllable	Millimeter-scale in width and depth; fish scale
Max Part Size	Limited by powder bed	Limited by powder bed	Very large (limited by robotic reach)
Material Compatibility	Wide (various alloys)	Conductive materials only	Wide (supports multi-material/FGM)
Primary DS/SX Application	Repair, small component fabrication	Direct fabrication of bulk SX components	Repair, large component cladding
Key Advantage in DS/SX	High resolution, fine features	Low residual stress, suitable for crack-sensitive alloys	High deposition rate, suitable for large parts repair
Key Limitation in DS/SX	High residual stress, cracking in sensitive alloys	Lower resolution, requires vacuum	Low resolution, poor surface finish
References	[42, 65, 78, 98–100]	[78, 100, 101]	[78, 100, 102–104]

pool dynamics, where the larger deposition volume and intense substrate interactions dominate grain evolution.

In L-PBF, common scan patterns include unidirectional raster, bidirectional zigzag, and interlayer rotation (e.g., 67° or 90°), alongside domain-based strategies like island/chessboard and hexagonal scanning (Figure 17) [108]. These designs do more than determine melt track overlap and heat accumulation; they fundamentally influence columnar grain growth direction and competitive outcomes by manipulating isotherm geometry and thermal gradient orientation [108–110].

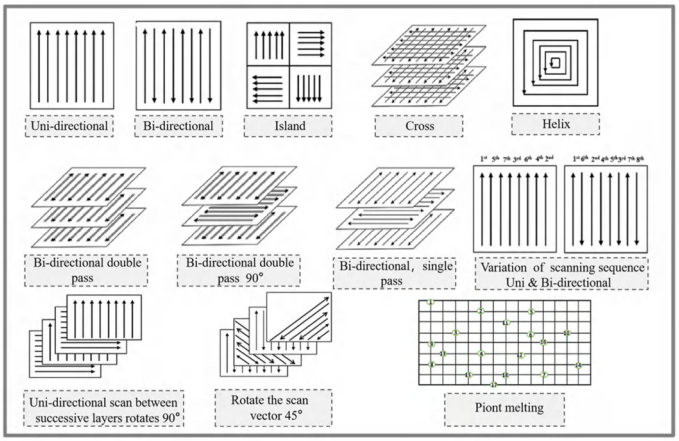

Figure 17. Common types of scanning strategies [109].

Systematic studies on alloys like IN718 demonstrate that simple unidirectional scanning promotes strongly textured columnar grains aligned with the build direction. Conversely, a 90° interlayer rotation encourages a cubic texture and weakens local alignment. Non-integer rotation angles, such as 67°, create complex heat-affected zone overlaps that increase the equiaxed grain fraction and further reduce texture intensity, a benefit for mitigating anisotropy, but a detriment to forming "quasi-SX" structures [111, 112].

Bidirectional zigzag scanning, by contrast, alternates the scan vector between adjacent tracks. This approach maintains a strong macroscopic columnar texture while reducing the thermal stress accumulation and distortion typical of unidirectional scanning, yielding spatially continuous and uniform columnar grains (Figure 18) [34].

Island or chessboard strategies partition the scan area into smaller domains to manage local heat buildup and global residual stress. Each island uses short scan vectors and is activated sequentially, allowing

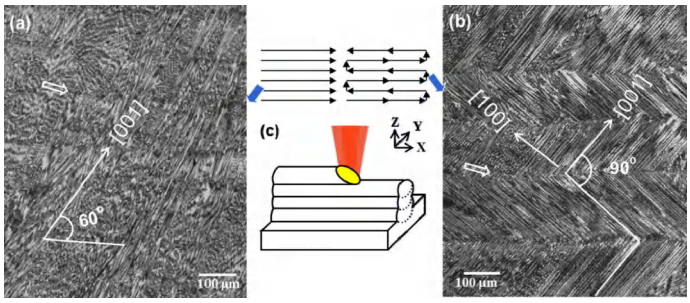

Figure 18. Solidification microstructures under different scanning strategies: (a) unidirectional scanning strategy and (b) bidirectional scanning strategy [34].

for "block-wise" thermal and stress management. Experiments and simulations confirm that smaller islands significantly reduce part warpage and residual deformation, while rapid thermal cycling within them refines grains. However, for DS and SX components, this grain refinement and the frequent rotation of scan vectors can be detrimental, as they inherently disrupt epitaxial continuity.

Island boundaries often suffer from complex textures and stress concentrations, requiring careful optimization of layout and sequence [113–115]. Beyond rectangular islands, hexagonal paths and segmented serpentine scans further homogenize these fields. For example, hexagonal paths in IN718 favor highly oriented columnar grains along the build axis, whereas chessboard patterns tend to induce equiaxed grains and cubic textures, directly undermining SX fidelity [116]. Island dimensions and sequencing also impact macroscopic mechanical properties: smaller islands produce finer grains, generally increasing yield strength at the cost of ductility [117]. Despite their benefits in stress mitigation, these complex strategies introduce significant crystallographic heterogeneity. Lu et al. [118] noted in Inconel 718 that while island scanning alleviates thermal accumulation, island overlap zones are prone to lack-of-fusion defects and porosity under fixed parameters, acting as preferred sites for stray grain nucleation and disrupting the uniform grain morphology essential for SX integrity.

Recently, fractal-based scan strategies defined by their continuity, lack of abrupt direction changes, non-intersecting paths, and self-similarity have gained traction. Fractal paths such as Hilbert and Peano-Gosper curves distribute heat uniformly and prevent localized reheating, effectively mitigating thermal stress concentrations. This results in substantially reduced crack density for highly crack-sensitive high-γ' superalloys [119]. As Figure 19

illustrates, crack length varies significantly between strategies, with fractal paths demonstrating superior crack resistance.

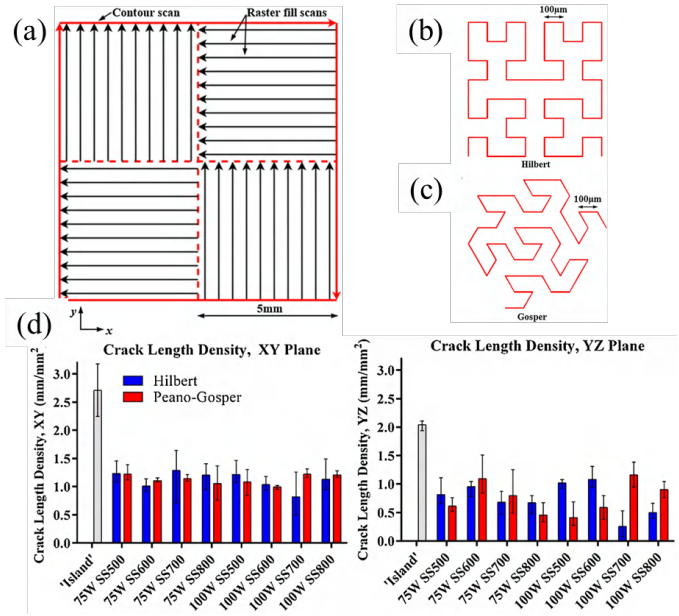

Figure 19. (a) Island scanning, (b) 3rd order Hilbert scan, (c) 2nd order Peano-Gosper scan, and (d) crack length density data for island (grey), Hilbert (blue), and Peano-Gosper (red) scan strategies [119].

In EB-PBF, the scan strategy evolves from a heat modulation tool into the core mechanism for SX formation. Leveraging the inertia-free deflection of the electron beam and the high-temperature preheated powder bed, scan paths dictate the local G/V ratio while enabling the deliberate construction of symmetric residual stress and temperature fields. Körner et al. [38] showed in CMSX-4 that μ-Helix-like paths can enforce a helical thermal gradient ascent, driving technical SX evolution. Through repeated competition and coalescence along the build height, columnar grains of varying orientations are filtered down to a single dominant orientation, forming SX domains several millimeters in diameter. Further simulations suggest that appropriate interlayer rotation in EB-PBF can maintain the primary [001] orientation parallel to the build direction while inducing continuous torsion of secondary orientations, a phenomenon termed "crystallographic twisting". This capability offers the potential to tailor crystallography for specific stress paths [120]. Essentially, this "unfolds" the traditional spiral grain selector into a 3D virtual selector shaped by thermal and stress fields, establishing scan strategy as the central tool for controlling SX/DS microstructures (Figure 20) [107].

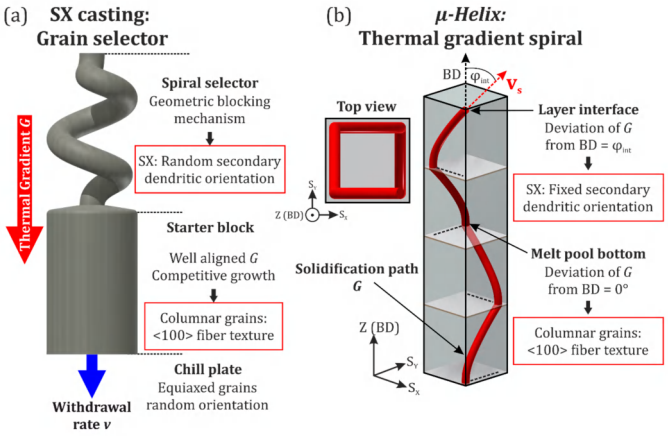

Figure 20. Path selection scanning [107].

4.2 Thermal Management and Preheating Effects

Thermal management is critical for controlling microstructure and defects in AM. By modulating part-to-substrate temperature gradients, preheating directly governs cooling rates, residual stress accumulation, and cracking susceptibility.

Standard L-PBF typically uses ambient-temperature substrates, inducing steep thermal gradients and residual stresses detrimental to high-γ' superalloys. Recent efforts focus on elevated substrate preheating (400–800 °C) to mitigate this. Research confirms that higher substrate temperatures reduce gradients and strain, effectively suppressing solidification and strain-age cracking (SAC). However, excessive preheating risks narrowing the densification window and promoting powder oxidation (Figure 21) [117].

In contrast, EB-PBF benefits inherently from high process temperatures. Pre-scan strategies maintain the powder bed near the γ' solvus, creating a high-temperature background that minimizes internal gradients and cooling rates relative to L-PBF. This thermal history not only mitigates hot tearing and shrinkage but also acts as an in situ heat treatment, promoting γ' coarsening and reprecipitation [121]. Recent simulation show that zonal and multi-stage preheating can further lower surface cooling rates. This compresses the liquation cracking range while preserving epitaxial growth, a critical requirement for crack-free SX fabrication of "unweldable" alloys like IN738 [122].

Thermal management in DED prioritizes substrate geometry and stiffness. While rigid substrates constrain initial distortion, they exacerbate stress accumulation during deposition, causing macroscopic warpage and cracking. Emerging "compliant" or

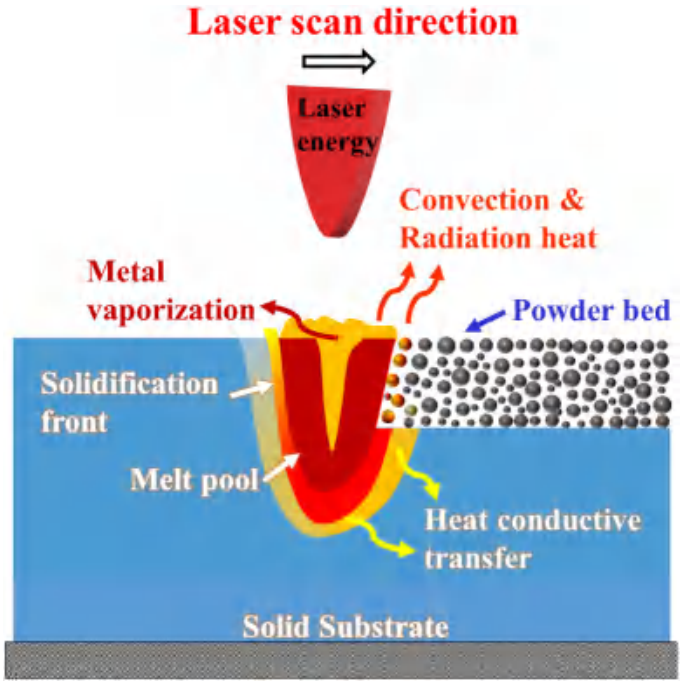

Figure 21. Schematic illustration of thermal phenomena occurring during L-PBF [117].

"smart" substrates, utilizing internal hollows, slots, or multi-material architectures, address this by reducing local stiffness. Both simulations and experiments confirm that these designs lower von Mises and longitudinal tensile stresses at the interface, inhibiting crack initiation and minimizing springback (Figure 22) [123].

In addition to stress management, thermal management fundamentally governs the CET and stray grain formation by spatiotemporally modulating G and V. In DED, aggressive cooling induces steep gradients and deep melt pools, triggering coarse equiaxed grains; compliant substrates or insulation mitigate this "first-layer shock" to facilitate stable epitaxy. In EB-PBF, preheating requires a trade-off: insufficient heat increases cracking risk, while excessive heat lowers the G/V ratio, weakening competitive growth and narrowing the SX formation window.

Rational thermal management is thus integral to process engineering. In L-PBF, this entails moderate preheating and optimized scanning to dampen thermal spikes. In EB-PBF, multi-stage preheating and real-time monitoring are required to balance crack suppression with directional solidification. Finally, in DED, tailoring substrate architecture alongside active cooling (e.g., forced cooling or slotting) is essential to reconcile stress control with microstructural homogeneity.

4.3 Energy Input Parameters and Melt Pool Geometry

In addition to scan strategy and thermal management, energy input parameters, specifically beam power (P), scan speed (v), hatch spacing (h), and layer thickness (t), fundamentally govern melt pool morphology and stability. While volumetric energy density (E_v) is a standard characterization metric [124].

$$E_v = \frac{P}{v \cdot h \cdot t} \tag{8}$$

It remains a simplified proxy. E_v remains widely used due to its simplicity and ease of comparison between different machines, but it cannot fully capture complex melt pool dynamics. For DS and SX control, melt-pool-geometry-based descriptors are more physically meaningful, as the curvature of the melt pool boundary directly dictates the local growth direction of the dendrites.

For DS and SX fabrication, the energy input must fall within a precise window that prevents lack-of-fusion defects without inducing keyhole instabilities. Low E_v leads to incomplete melting and porosity, whereas excessive E_v drives keyhole formation, vapor recoil, and spatter, all of which disrupt epitaxial continuity. Consequently, SX/DS processes prioritize the conduction-mode regime, utilizing high G and moderate V to sustain columnar growth while mitigating stress accumulation through scan optimization and preheating [125].

The response of G and V to P, v, and beam diameter (D) is nonlinear. Increasing power deepens the melt pool. While deep, narrow pools exhibit high local G, they are prone to constitutional supercooling at the pool bottom, risking stray grain nucleation. Conversely, shallow, wide pools generate gentler gradients favorable for stable, long-range epitaxy. Adjusting scan speed alters the energy deposition rate. At low speeds, the rise in V typically lowers the G/V ratio, whereas at higher speeds, melt pool shallowing enhances G relative to V, thereby shifting the balance back toward columnar growth [117].

Beam spot size and intensity profiles offer further geometric control. Small Gaussian spots concentrate energy, creating deep pools with steep gradients and strong Marangoni convection, which can coarsen dendrites or trigger equiaxed growth. In contrast, larger Gaussian or flat-top profiles produce wider, shallower pools with more uniform thermal fields,

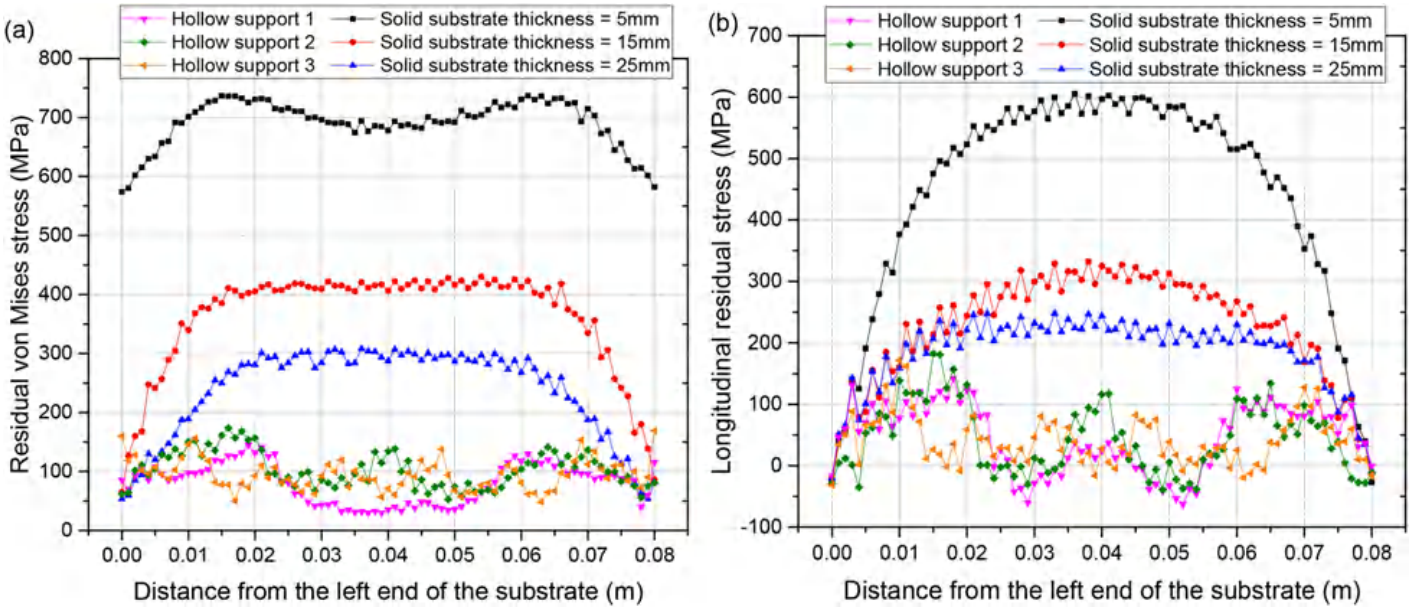

Figure 22. Residual stress distribution at the wall-substrate interface for different substrate structures: (a) von Mises stress; (b) longitudinal stress [123].

extending the stability range of the columnar zone (Figure 23) [126–128]. Research on Fe-Si [129] and Ni-based alloys [122] in L-PBF and laser cladding confirms that expanding the spot size broadens the conduction-mode window, suppressing keyholing and enhancing microstructural continuity.

Operational strategies for SX/DS must therefore reconcile the high G required for epitaxy with the need to minimize thermal stress. In L-PBF, this entails moderate power, high scan speed, and slightly enlarged spot sizes to reduce peak thermal gradients while ensuring densification. In EB-PBF, line energy and dwell time are tuned against a high-temperature background to maintain directional growth without compromising. In DED, success relies on limiting thermal and mass input to achieve shallow, elongated melt pools, thereby preventing stray grains nucleated at the pool base.

Ultimately, energy input, scan strategy, and thermal management constitute the triad of process control in AM. By collectively shaping melt pool geometry, G and V, they dictate the columnar-to-equiaxed transition, grain orientation, and defect genesis. Achieving robust SX/DS structures requires moving beyond trial-and-error to a systematic methodology grounded in coupled thermo-mechanical-microstructural modeling.

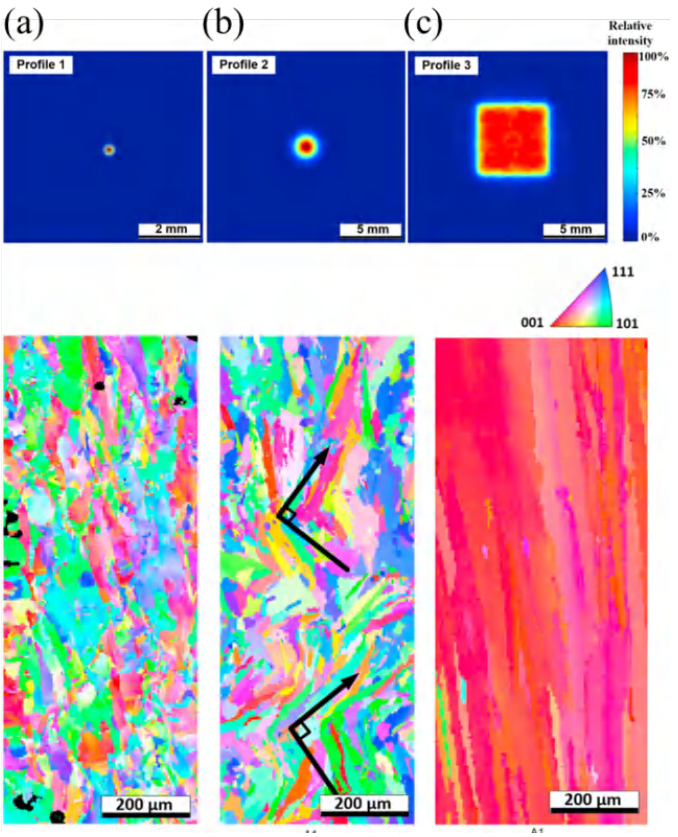

Figure 23. Grain morphology of Inconel 718 alloy fabricated by selective laser melting with different laser beam energy distributions [126].

5 Defect Mitigation and Hybrid Synergy in High-γ' Superalloys

Defect mitigation in high-γ' superalloys represents a multi-physics challenge that extends beyond

the capabilities of conventional process mapping. The substantial thermal stresses induced during layer-wise accumulation, coupled with the alloy's rapid precipitation kinetics, create a propensity for both intergranular cracking and the disruption of epitaxial growth (stray grains). Addressing these issues requires a rigorous deconstruction of the failure modes governing porosity evolution and surface degradation. Furthermore, as singular process optimization often reaches a theoretical limit, this section posits hybrid synergy as a requisite solution pathway. Through the convergence of multi-source processing and active microstructure control, hybrid strategies offer a means to manipulate local solidification dynamics, effectively suppressing defect formation while maintaining the desired crystallographic texture.

5.1 Stray Grain Nucleation and Suppression

SGs pose a critical threat to the crystallographic integrity of SX components, manifesting as misoriented defects that degrade creep and fatigue performance. Unlike in traditional casting, where SGs are typically localized to component edges, AM-induced SGs exhibit complex spatial distributions, appearing near substrates, within deposited layers, and on surfaces [82, 130]. Their formation is primarily driven by constitutional undercooling, grain fragmentation, and heterogeneous nucleation.

Mechanistically, SGs near the substrate often arise from the partial remelting of coarse precipitates (e.g., carbides, γ/γ' eutectics), which serve as nucleation sites for equiaxed grains once the local ratio drops into the regime that favors CET. Within the build, repeated thermal cycling can trigger recrystallization in high-strain zones, while surface SGs frequently originate from incompletely melted powder particles that act as extrinsic nuclei [82].

Mitigation strategies target both source elimination and process suppression. Pre-processing measures, such as solution heat treatment of substrates, dissolve segregation-prone phases to reduce constitutional undercooling, while rigorous powder quality control minimizes extrinsic inclusions. During fabrication, maintaining a high ratio delays CET, and optimizing scan strategies, such as employing bidirectional paths, preserves epitaxial continuity by minimizing local powder accumulation and undercooling (Figure 24) [130].

In EB-PBF, this approach is refined through high-temperature preheating and "virtual grain selection" scan patterns, which promote competitive grain growth to confine SGs to the periphery, effectively self-purifying the bulk crystal. Ultimately, controlling SGs requires the coordinated regulation of material quality, thermal fields, and scanning dynamics across multiple scales.

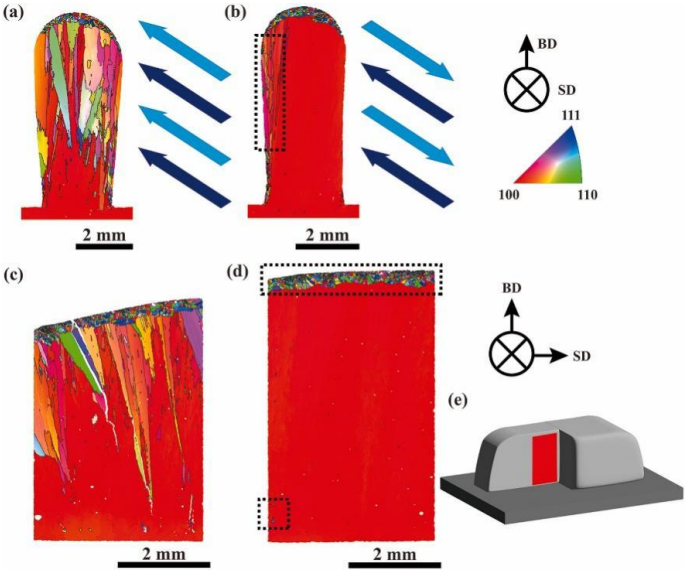

Figure 24. EBSD orientation maps of samples built using different scanning strategies:(a) and (c) Unidirectional laser scanning; (b) and (d) Bidirectional laser scanning. (c) and (d) are from the center of the sample shown in Figure (e) [130].

5.2 Mechanism and Control of Cracks

In the AM of high-γ' superalloys, cracking remains a persistent challenge that severely restricts the process window and compromises component reliability. Analogous to welding, cracking in AM can be categorized into three primary types: solidification cracking, liquation cracking, and solid-state cracking, with the latter further subdivided into SAC and ductility-dip cracking (DDC).

Solidification cracking occurs predominantly within interdendritic channels during the final stages of solidification. As depicted in Figure 25 [131], rapid cooling drives the segregation of γ'-forming elements (Al, Ti) and refractory alloying elements (Nb, Mo, W, Re) into interdendritic regions, forming low-melting γ-γ' eutectics or solute-rich liquid films. Under non-equilibrium solidification, these compositional gradients cannot homogenize. Consequently, the semi-solid dendritic network is subjected to tensile stresses arising from thermal contraction and mechanical constraint. When these stresses exceed the cohesive strength of the residual liquid films,

interdendritic tearing occurs, manifesting as classic solidification cracks [132]. Studies on IN738 and CM247LC processed via DED and L-PBF confirm that such defects typically appear as coarse intergranular fractures accompanied by pronounced segregation and ruptured dendrites [133, 134].

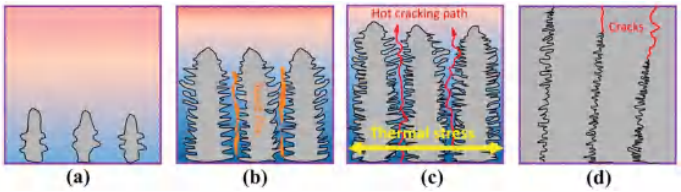

Figure 25. Schematic illustration of solidification cracking mechanisms [131].

Constitutional liquation occurs when rapid heating in AM and welding causes solutes to concentrate at the precipitate/matrix interface in HAZs. As the local temperature and solute concentration reach eutectic equilibrium, metastable liquid films are generated; when these reach a certain areal density, they combine to form large films that result in cracking. Simultaneously, low-melting-point secondary precipitates such as γ'-γ eutectic, γ-Laves eutectic, and carbides contribute to cracking as they directly melt during heating cycles [131].

Liquation cracking is most prevalent in the heat-affected zone or remelted regions. Repeated thermal cycling causes low-melting interdendritic phases, such as γ-γ' eutectics, B-rich borides (e.g., M_5B_3, M_3B_2), and carbides (MC, M_6C), to partially melt. This results in the formation of continuous or semi-continuous liquid films along grain boundaries or secondary dendrite arms. Just below the liquidus temperature, these films exist in a semi-solid state with negligible ductility. Tensile stresses induced by thermal cycling can then propagate cracks along these weakened interfaces [135]. The two primary mechanisms, constitutional liquation and direct phase melting, are schematically illustrated in Figure 26.

Investigations on René 108 and similar alloys demonstrate that adjusting preheating temperature and heating rate can shift both the onset and width of the liquation cracking temperature range (LCTR), thereby modulating susceptibility [131, 136].

SAC poses a significant risk for high-γ' superalloys such as CM247LC and IN939, which typically exhibit γ' volume fractions exceeding 60%. During the multiple thermal cycles inherent to AM, extensive γ' precipitation and coarsening occur. The lattice

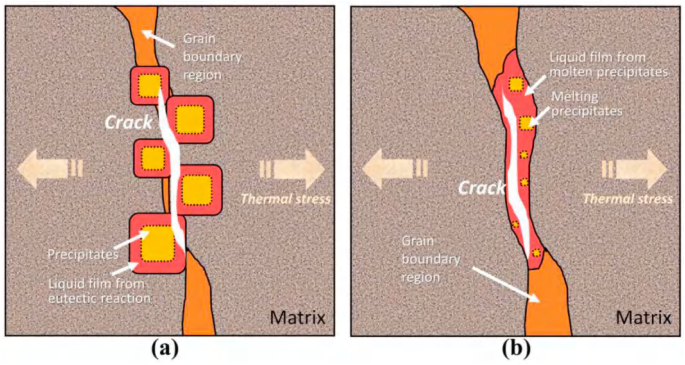

Figure 26. Schematic of the liquation cracking caused by (a) constitutional liquation and (b) direct phase melting [131].

mismatch between the γ and γ' phases, coupled with volumetric expansion during precipitation, generates localized stress concentrations at grain boundaries. Simultaneously, γ' hardening reduces material ductility.

The superposition of residual stress and precipitation hardening can thus trigger intergranular fracture. Fractographic analysis reveals these cracks as sharp, intergranular features lacking any evidence of dendritic melting, often traversing multiple melt pools, which is a key distinction from solidification or liquation cracks (Figure 27) [71, 137].

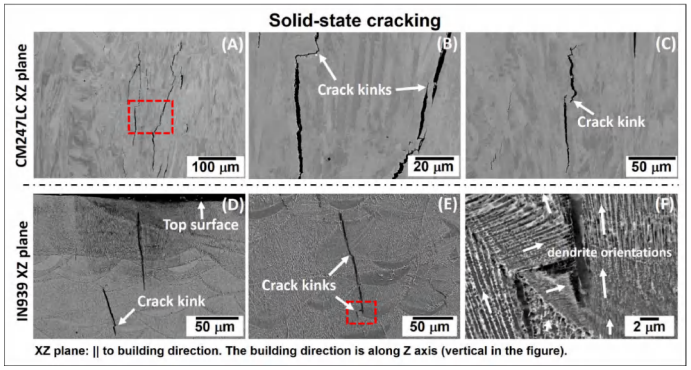

Figure 27. Strain-age cracking in CM247LC (a–c) and IN939 (d–f) [71].

Mitigating these cracking modes requires integrated strategies spanning process control and material design. For solidification cracking, tuning energy density, scan speed, and preheat conditions can reduce interdendritic segregation and the volume fraction of low-melting phases, shorten terminal liquid films, and minimize tensile stress concentrations through optimized scan strategies such as island scanning, bidirectional serpentine patterns, or multi-directional scanning. Statistical analyses of CM247LC indicate that maintaining linear energy input within an optimal range and avoiding deep keyhole-mode melt pools

significantly reduces crack density [138].

For liquation cracking, optimizing preheat temperature and thermal history is critical. Techniques such as high-frequency induction heating and multi-stage preheating can modify the HAZ microstructure prior to deposition or AM, rendering low-melting phases more discontinuous. This narrows the LCTR and reduces susceptibility, a strategy validated in both René 108 welding and EB-PBF of IN738LC.

Addressing SAC and DDC requires harmonizing heat treatment protocols with residual stress management. Precise control over heating rates and hold temperatures is essential to regulate γ' precipitation kinetics, thereby optimizing instantaneous ductility and reducing local stress concentrations. At the process level, interventions such as staged heat treatments, compliant fixturing, and in-process annealing effectively alleviate strain accumulation within critical temperature intervals. Furthermore, emerging techniques like Liquid-Phase-Induced Healing (LIH) and laser remelting provide pathways to restore metallurgical continuity by locally healing crack tips, a strategy successfully validated in L-PBF CM247LC components [139, 140]

Fundamentally, cracking reflects the intrinsic conflict between the high thermal G/V ratio required for columnar epitaxy and the low residual stress state needed to suppress fracture. While L-PBF, EB-PBF, and DED occupy different positions along this trade-off spectrum, successful fabrication demands the unified co-design of solidification behavior, thermal stress evolution, and γ' precipitation dynamics.

5.3 Internal Porosity and Surface Integrity

Beyond cracking, porosity and surface roughness represent critical defects in high-γ' superalloys. These defects not only compromise load-bearing capacity but also act as potent stress concentrators, initiating fatigue failure and degrading cooling efficiency in complex turbine components.

5.3.1 Morphological Influence of Internal Porosity on Mechanical Performance

Internal porosity in metal AM primarily consists of lack of fusion (LOF), gas, keyhole, and shrinkage pores [141]. The impact of these defects on mechanical performance depends on their morphology, orientation, and proximity to the surface.

Lack-of-fusion pores, characterized as flattened, irregular voids containing unmelted powder, arise from insufficient energy input or inadequate melt pool overlap. In DS or SX structures, these defects often align with scan tracks or layer interfaces, running parallel to grain boundaries and serving as high-intensity crack initiation sites under creep or fatigue loading [142]. Studies on Ni–Cr–Fe superalloys demonstrate that below the densification threshold, relative density drops precipitously due to LOF defects, which almost invariably function as fatigue fracture origins [143].

Conversely, gas and keyhole porosity have markedly different effects on mechanical performance. Gas porosity typically consists of spherical pores ranging from several to tens of micrometers in diameter [144]. These defects primarily impair high-cycle fatigue life, particularly when located in subsurface regions. Fatigue failures in L-PBF nickel-based superalloys at 10^7 cycles predominantly initiate at these sites, with life exhibiting a strong inverse correlation with maximum pore size [145].

Keyhole porosity is characteristic of high-energy-density regimes where vapor cavities collapse [146–148]. These defects result in a sharp increase in porosity that markedly degrades both fatigue and impact toughness [149], even at high bulk densities. While gas pores are often viewed as passive inclusions, the irregular morphology of keyhole porosity creates significantly higher local stress triaxiality, making it more detrimental to dynamic properties. In contrast, the high-vacuum environment of EB-PBF drastically reduces gaseous sources, routinely achieving bulk densities of 99.98% (Figure 28), although minor spherical porosity may still arise from residual adsorbed or internal gases in the powder [150].

Additionally, interdendritic micropores associated with restricted solidification feeding persist in DED or EB-PBF. These pores often co-locate with segregation bands and serve as nucleation sites for creep cavitation. While HIP effectively closes internal micropores through synergistic plastic flow and diffusion [151, 152], it is significantly less effective for interconnected LOF pores or large keyhole voids open to the surface [153]. Consequently, the optimal strategy requires minimizing LOF and keyhole porosity through process optimization to ensure residual defects consist only of healable micropores.

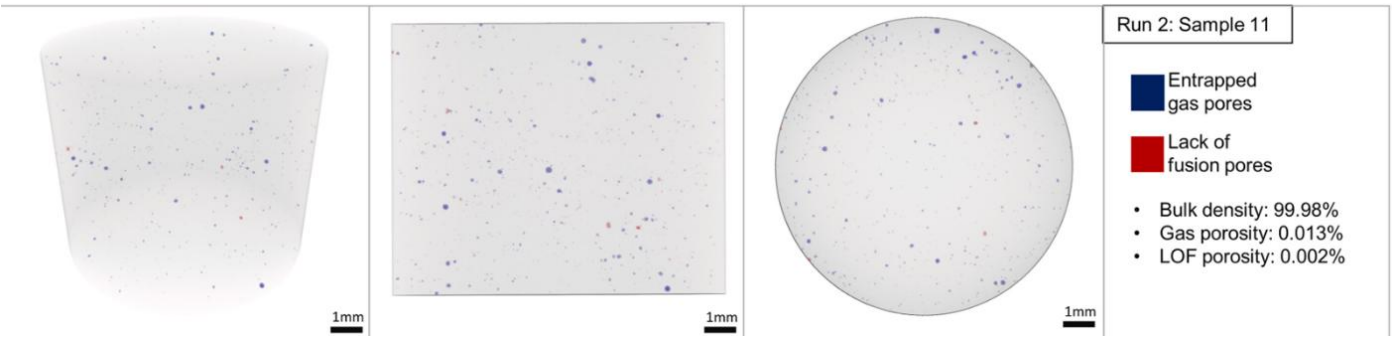

Figure 28. Three-dimensional reconstruction and classification distribution of internal pore defects in samples using Micro-CT [150].

5.3.2 *Functional Implications of Surface Integrity and Post-Processing*

Surface integrity represents the second critical challenge in AM [154]. The layer-wise process inherently induces stair-stepping effects on external surfaces (Figure 29) [15], while internal channels suffer from adhered powder and localized overmelting due to geometric confinement. This roughness, significantly higher than that of cast components, degrades cooling efficiency and serves as a potent site for fatigue crack initiation [155]. Consequently, post-processing is mandatory [156]. While conventional machining is sufficient for external features, internal passages require volumetric techniques such as electrochemical polishing (ECP).

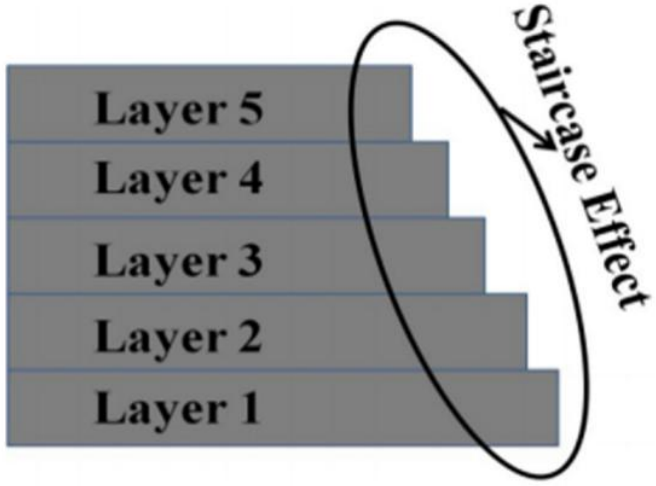

Figure 29. Schematic illustration of the staircase effect in layer-based manufacturing [15].

In EB-PBF, small hatch spacing often leads to the sintering of surrounding powder onto channel walls, yielding highly undulating topographies [157]. Conversely, in L-PBF, high energy density combined with tight hatch spacing increases sidewall roughness, though this can be mitigated by energy reduction or contour scanning [158].

To address these issues, techniques such as ECP, electrochemical–mechanical hybrid polishing (ECMP), and abrasive flow finishing (AFF) can significantly reduce areal surface roughness (Sa) while preserving geometric fidelity. For IN625, optimized ECP reduces inner roughness by 60–85%, albeit with a 5–15% wall thickness loss [159]. Emerging methods, including magnetic abrasive finishing (MAF) and multi-nozzle hydrodynamic polishing, show promise for small-diameter or multi-layer channels but entail higher process complexity [160]. As shown in Figure 30, the effectiveness of these methods varies significantly with channel geometry and material systems, indicating that no single technique is universally optimal [161].

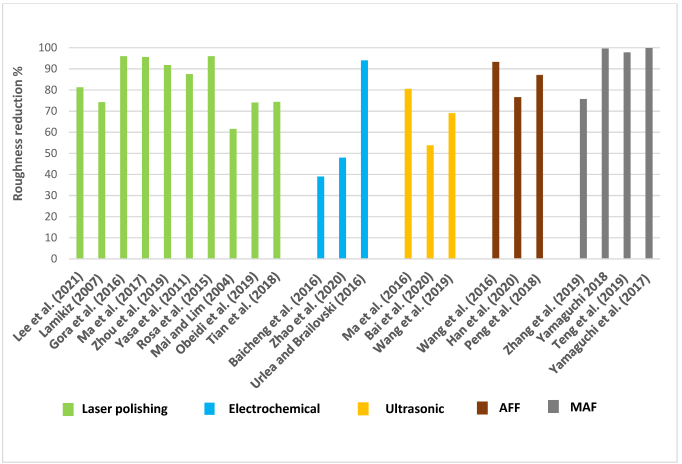

Figure 30. Schematic illustration of the staircase effect in layer-based manufacturing [161].

For SX or DS blades, enhancing surface integrity is particularly delicate. Strategies such as laser remelting risk altering the near-surface microstructure or triggering recrystallization. Therefore, co-optimization of AM process design and post-processing is essential to maintain

crystallographic continuity while achieving the desired surface finish. This integrated approach is critical for transitioning AM components from laboratory prototypes to high-reliability aerospace applications.

5.4 Hybrid Synergy Strategies: Processing High-γ' Superalloys

For legacy high-γ' systems such as CMSX-4 and IN738, relying solely on parametric optimization proves insufficient to eliminate cracking and stray grain nucleation. Addressing these intrinsic metallurgical constraints necessitates a paradigm shift toward Hybrid Synergy, which represents the strategic integration of process physics, alloy chemistry, and auxiliary fields. From a process-driven perspective, EB-PBF exploits a thermal process window inaccessible to laser-based systems. By maintaining the powder bed temperature near the γ' solvus, the process minimizes the thermal stress invariant while sustaining the high G required for directional growth. This specific thermal regime effectively "unlocks" the printability of crack-sensitive alloys, enabling the direct fabrication of defect-free, seedless single crystals which, following HIP and heat treatment, exhibit creep and tensile properties commensurate with their cast counterparts. Complementing this process-centric approach, L-PBF strategies increasingly prioritize compositional compliance. Since the process lacks the high-temperature background of EB-PBF, the alloy itself must be engineered for rapid solidification. The development of SD247 from the legacy CM247LC precursor exemplifies this trend: by rebalancing γ'-forming elements and optimizing grain-boundary strengtheners (e.g., C, B, Hf), researchers have successfully expanded the freezing range tolerance, demonstrating that alloy chemistry can be fundamentally re-engineered to accommodate extreme cooling rates without sacrificing high-temperature performance [162].

Beyond primary processing, hybrid approaches extend to the integration of external fields and restorative post-processing to ensure structural integrity. LIH offers a mechanism to repair process-induced microcracks by transiently generating a semi-solid zone, allowing capillary forces to backfill voids and re-establish metallurgical continuity via localized epitaxial solidification. Furthermore, the incorporation of active auxiliary fields, such as high-frequency induction heating during DED, dynamically modifies the thermal history. For alloys like René 108, induction preheating alters the morphology of low-melting phases in the heat-affected zone, effectively widening the crack-free deposition window. Ultimately, "AM manufacturability" is evolving from a passive constraint into an active design criterion. The future of high-temperature AM lies in the construction of multi-dimensional design spaces that correlate composition, solidification dynamics, and defect susceptibility, with the goal of developing AM-Specific High-γ' Superalloys, materials designed not merely to survive the printing process but to leverage its unique thermal history for superior performance.

6 Conclusion and Outlook

AM has redefined many limitations of traditional directional solidification processes in regulating metal crystal structures, offering geometric freedom and integration capabilities far beyond conventional investment casting for achieving DS, quasi-SX, and SX microstructures in complex three-dimensional geometries. As elucidated in this review, the fabrication of high-γ' nickel-based superalloys relies on mastering solidification dynamics across three complementary platforms: For nickel-based superalloys, L-PBF, EB-PBF, and DED now form a complementary triad: L-PBF excels in fabricating high-resolution cooling features and engineering quasi-SX textures; DED enables large-scale quasi-SX construction and epitaxial repair of critical regions such as blade tips, maintaining single-crystal or highly directional columnar epitaxy over tens of millimeters when guided by process window maps and melt pool orientation models; and EB-PBF, leveraging high-temperature powder bed preheating and a high-vacuum environment, provides the most promising route to directly produce large SX/DS components from high-γ' superalloys such as CMSX-4, IN738, and M247, yielding multi-millimeter SX regions or even technical single crystals without single-crystal substrates, with creep and tensile properties after HIP and optimized heat treatment approaching or exceeding those of cast counterparts.

Despite these advances, challenges persist. An incomplete understanding of epitaxial stability and grain competition (specifically the Stray Grain and CET mechanisms) hinders reproducibility. Furthermore, while EB-PBF mitigates cracking, it suffers from surface roughness and powder entrapment in intricate channels—limitations where

L-PBF remains indispensable.

To overcome the trilemma of "printability, performance, and geometric complexity," the future of AM for high-temperature single crystals lies in Hybrid Synergy. We propose a paradigm shift where isolated processes evolve into an integrated ecosystem: utilizing EB-PBF as the structural core for the defect-free SX matrix, augmented by L-PBF for intricate cooling features, DED for epitaxial features or repair, and subtractive finishing for surface integrity. To transition this framework from "formable" to "certifiable," four critical frontiers must be advanced:

1. Predictive Process Control: Shift from empirical process windows to quantitative process–structure–property mappings. Integrating multi-physics modeling with in-situ monitoring will enable predictive control over microstructural evolution.
2. AM-Specific Alloy Design: Move beyond adapting cast alloys to designing AM-Specific superalloys. Compositional optimization must balance printability with high-temperature performance using multi-dimensional design maps.
3. Intelligent Closed-Loop Systems: Implement adaptive control via machine learning. Correlating real-time melt pool data with target microstructural features will enable robust, microstructure-driven regulation.
4. Lifecycle Certification: Establish certification paradigms tailored to AM. New frameworks must address coupled damage modes (creep–fatigue–corrosion) to close the manufacturing–service–repair loop.

In summary, EB-PBF should be viewed as a "structural platform" rather than a standalone process. Integrating it with L-PBF, DED, and intelligent monitoring creates a flexible toolkit essential for the engineering implementation of complex SX components.

Data Availability Statement

Not applicable.

Funding

This work was supported in part by the National Natural Science Foundation of China under Grant 52202049; in part by the Fundamental Research Funds for the Central Universities under Grant 30924010206; in part by the Advanced Materials-National Science and Technology Major Project under Grant 2025ZD0608601.

Conflicts of Interest

The authors declare no conflicts of interest.

AI Use Statement

The authors declare that no generative AI was used in the preparation of this manuscript.

Ethical Approval and Consent to Participate

Not applicable.

References

[1] Zhao, Y. S., Zhang, J., Luo, Y. S., Zhang, B., Sha, G., Li, L. F., ... & Feng, Q. (2019). Improvement of grain boundary tolerance by minor additions of Hf and B in a second generation single crystal superalloy. *Acta Materialia, 176*, 109-122. [CrossRef]

[2] Popli, D., Batra, U., Msomi, V., & Verma, S. (2023). A systematic survey of RUM process parameter optimization and their influence on part characteristics of nickel 718. *Scientific Reports, 13*(1), 1716. [CrossRef]

[3] Takeishi, K. (2022). Evolution of turbine cooled vanes and blades applied for large industrial gas turbines and its trend toward carbon neutrality. *Energies, 15*(23), 8935. [CrossRef]

[4] Langston, L. (2015). Each blade a single crystal. *American Scientist, 103*(1), 30. [CrossRef]

[5] Abdallah, S., Ali, S., Pervaiz, S., & Kannan, S. (2022). Conventional machining of single crystal metals and super alloys: A review. *Journal of Manufacturing Science and Engineering, 144*(9), 090801. [CrossRef]

[6] Ma, D. (2018). Novel casting processes for single-crystal turbine blades of superalloys. *Frontiers of Mechanical Engineering, 13*(1), 3–16. [CrossRef]

[7] Hallensleben, P., Schaar, H., Thome, P., Jöns, N., Jafarizadeh, A., Steinbach, I., ... & Frenzel, J. (2017). On the evolution of cast microstructures during processing of single crystal Ni-base superalloys using a Bridgman seed technique. *Materials & Design, 128*, 98-111. [CrossRef]

[8] Dong, R. Z., Wang, W., Wang, Y., Zhang, T. R., Jiang, R., & Cui, K. (2023). Machine learning-enabled early prediction of dimensional accuracy for complex products of investment casting. *Research Square*. [CrossRef]

[9] Carter, P., Cox, D. C., Gandin, C. A., & Reed, R. C. (2000). Process modelling of grain selection during

the solidification of single crystal superalloy castings. *Materials Science and Engineering: A, 280*(2), 233–246. [CrossRef]

[10] Groover, M. P. (2010). *Fundamentals of modern manufacturing: Materials, processes, and systems*. John Wiley & Sons.

[11] Chyu, M. K., & Siw, S. C. (2013). Recent advances of internal cooling techniques for gas turbine airfoils. *Journal of Thermal Science and Engineering Applications, 5*(2), 021008. [CrossRef]

[12] Yan, S., Shi, J., Li, G., Hao, C., Wang, Y., Yu, H., & Zhou, W. (2024). Advances in Aeroengine Cooling Hole Measurement: A Comprehensive Review. *Sensors, 24*(7), 2152. [CrossRef]

[13] Xu, L., Sun, Z., Ruan, Q., Xi, L., Gao, J., & Li, Y. (2023). Development Trend of Cooling Technology for Turbine Blades at Super-High Temperature of above 2000 K. *Energies, 16*(2), 668. [CrossRef]

[14] Angel, N. M., & Basak, A. (2020). On the Fabrication of Metallic Single Crystal Turbine Blades with a Commentary on Repair via Additive Manufacturing. *Journal of Manufacturing and Materials Processing, 4*(4), 101. [CrossRef]

[15] Sinha, A., Swain, B., Behera, A., Mallick, P., Samal, S. K., Vishwanatha, H. M., & Behera, A. (2022). A review on the processing of aero-turbine blade using 3D print techniques. *Journal of manufacturing and materials processing, 6*(1), 16. [CrossRef]

[16] Shen, W., Zhang, P., Li, W., & Qin, H. (2025). Additive manufacturing for functional design: a review of capabilities, strategies and applications. *Rapid Prototyping Journal*, 1-27. [CrossRef]

[17] Thomas, D. (2016). Costs, benefits, and adoption of additive manufacturing: A supply chain perspective. *The International Journal of Advanced Manufacturing Technology, 85*(5), 1857–1876. [CrossRef]

[18] Tofail, S. A., Koumoulos, E. P., Bandyopadhyay, A., Bose, S., O'Donoghue, L., & Charitidis, C. (2018). Additive manufacturing: Scientific and technological challenges, market uptake and opportunities. *Materials Today, 21*(1), 22–37. [CrossRef]

[19] Yang, S., & Zhao, Y. F. (2015). Additive manufacturing-enabled design theory and methodology: A critical review. *The International Journal of Advanced Manufacturing Technology, 80*(1), 327–342. [CrossRef]

[20] Haines, M. P., Rielli, V. V., Primig, S., & Haghdadi, N. (2022). Powder bed fusion additive manufacturing of Ni-based superalloys: A review of the main microstructural constituents and characterization techniques. *Journal of Materials Science, 57*(30), 14135–14187. [CrossRef]

[21] Gong, L., Li, Y. B., Wang, X. P., Li, S., Yang, Z. G., & Chen, H. (2025). Progress in additive manufacturing of nickel-based superalloys: materials, processing, microstructures, properties and alloy design: L. Gong et al. *Rare Metals, 44*(10), 7041-7087. [CrossRef]

[22] Agapovichev, A. V., Khaimovich, A. I., Smelov, V. G., Kokareva, V. V., Zemlyakov, E. V., Babkin, K. D., & Kovchik, A. Y. (2023). Multiresponse Optimization of Selective Laser Melting Parameters for the Ni-Cr-Al-Ti-Based Superalloy Using Gray Relational Analysis. *Materials, 16*(5), 2088. [CrossRef]

[23] Quan, Z., Jia, Q., Zhang, Z., Wang, Y., Ma, L., Hu, Q., & Guo, F. (2025). Composition design for laser powder bed fusion (LPBF) fabricated Ni-based superalloys: A review. *Journal of Manufacturing Processes, 155*, 119–136. [CrossRef]

[24] Ghiaasiaan, R., Poudel, A., Ahmad, N., Gradl, P. R., Shao, S., & Shamsaei, N. (2022). High temperature tensile and fatigue behaviors of additively manufactured IN625 and IN718. *Procedia Structural Integrity, 38*, 581–587. [CrossRef]

[25] Wu, B., Gao, H., Huang, Y., Li, S., Chen, Z., Li, W., ... & Wei, Q. (2025). Comparative study of dot-ring and Gaussian beams on epitaxial grain growth and crack suppression of DD6 superalloy fabricated by laser powder bed fusion. *Materials Science and Engineering: A, 923*, 149181. [CrossRef]

[26] Huang, R., Shi, W., Xu, K., Wang, R., Xie, H., & Wei, K. (2025). The influence of process parameters and building orientation on fracture toughness and fatigue crack growth behavior of laser powder bed fused tantalum. International Journal of Fatigue, 199, 109086. [CrossRef]

[27] Chen, Y., Wang, W., Ou, Y., Li, D., Chang, H., Wu, Y., Yang, R., Zhai, Z., & Li, C. (2023). Effect of high preheating on the microstructure and mechanical properties of high gamma prime Ni-based superalloy manufactured by laser powder bed fusion. *Journal of Alloys and Compounds, 960*, 170598. [CrossRef]

[28] Li, Y., Long, H., Wei, B., Zhou, J., & Lin, F. (2024). Multiple preheating processes for suppressing liquefaction cracks in IN738LC superalloy fabricated by electron beam powder bed fusion (EB-PBF). *Materials, 17*(22), 5667. [CrossRef]

[29] Lu, X., Zhang, G., Chiumenti, M., Cervera, M., Wang, Z., Yao, B., & Lin, X. (2025). Additive manufacturing of crack-free large IN738LC parts through tailored substrate designs. *Thin-Walled Structures, 210*, 112979. [CrossRef]

[30] Pham, M. S., Dovgyy, B., Hooper, P. A., Gourlay, C. M., & Piglione, A. (2020). The role of side-branching in microstructure development in laser powder-bed fusion. *Nature communications, 11*(1), 749. [CrossRef]

[31] Wang, G., Ouyang, H., Fan, C., Guo, Q., Li, Z., Yan, W., & Li, Z. (2020). The origin of high-density dislocations in additively manufactured metals. *Materials Research Letters, 8*(8), 283–290. [CrossRef]

[32] Basak, A., & Das, S. (2016). Epitaxy and microstructure evolution in metal additive manufacturing. *Annual Review of Materials Research,*

46(1), 125-149. [CrossRef]

[33] Li, Y., Liang, X., Yu, Y., Wang, D., & Lin, F. (2022). Review on additive manufacturing of single-crystal nickel-based superalloys. *Chinese Journal of Mechanical Engineering: Additive Manufacturing Frontiers, 1*(1), 100019. [CrossRef]

[34] Liu, Y., & Shi, J. (2023). Epitaxial growth and stray grain control toward single-crystal metallic materials by additive manufacturing: a review. *Advanced Engineering Materials, 25*(14), 2201917. [CrossRef]

[35] Wu, H., Zhou, J., Huang, L., Wang, Z., Tan, L., Lv, J., & Liu, F. (2025). Advances in Crack Formation Mechanisms, Evaluation Models, and Compositional Strategies for Additively Manufactured Nickel-Based Superalloys. *Computer Modeling in Engineering & Sciences, 143*(3), 2675–2709. [CrossRef]

[36] Yang, J., Li, F., Pan, A., Yang, H., Zhao, C., Huang, W., ... & Zhang, X. (2019). Microstructure and grain growth direction of SRR99 single-crystal superalloy by selective laser melting. *Journal of Alloys and Compounds, 808*, 151740. [CrossRef]

[37] Boswell, J. H., Clark, D., Li, W., & Attallah, M. M. (2019). Cracking during thermal post-processing of laser powder bed fabricated CM247LC Ni-superalloy. *Materials & Design, 174*, 107793. [CrossRef]

[38] Körner, C., Ramsperger, M., Meid, C., Bürger, D., Wollgramm, P., Bartsch, M., & Eggeler, G. (2018). Microstructure and mechanical properties of CMSX-4 single crystals prepared by additive manufacturing. *Metallurgical and Materials Transactions A, 49*(9), 3781-3792. [CrossRef]

[39] Liu, L., Wang, D., Deng, G., Liu, Z., Tan, C., Zhou, X., Han, C., Jiang, R., & Yang, Y. (2023). Crack inhibition to enhance strength-ductility of CM247LC alloy fabricated by laser powder bed fusion. *Materials Science and Engineering: A, 875*, 145114. [CrossRef]

[40] Liu, L., Huang, T., Qu, M., Liu, G., Zhang, J., & Fu, H. (2010). High thermal gradient directional solidification and its application in the processing of nickel-based superalloys. *Journal of Materials Processing Technology, 210*(1), 159–165. [CrossRef]

[41] Martin, A. A., Calta, N. P., Hammons, J. A., Khairallah, S. A., Nielsen, M. H., Shuttlesworth, R. M., ... & Lee, J. R. (2019). Ultrafast dynamics of laser-metal interactions in additive manufacturing alloys captured by in situ X-ray imaging. *Materials Today Advances, 1*, 100002. [CrossRef]

[42] Liu, Z., Zhou, Q., Liang, X., Wang, X., Li, G., Vanmeensel, K., & Xie, J. (2024). Alloy design for laser powder bed fusion additive manufacturing: a critical review. *International Journal of Extreme Manufacturing, 6*(2), 022002. [CrossRef]

[43] Karimi, P., Sadeghi, E., Ålgårdh, J., Keshavarzkermani, A., Esmaeilizadeh, R., Toyserkani, E., & Andersson, J. (2021). Columnar-to-equiaxed grain transition in powder bed fusion via mimicking casting solidification and promoting in situ recrystallization. *Additive Manufacturing, 46*, 102086. [CrossRef]

[44] Kurz, W., Fisher, D. J., & Rappaz, M. (2023). *Fundamentals of solidification* (5th ed.). Trans Tech Publications Ltd.

[45] Das, S. (2003). Physical Aspects of Process Control in Selective Laser Sintering of Metals. *Advanced Engineering Materials, 5*(10), 701–711. [CrossRef]

[46] Grong, Ø. (1997). *Metallurgical modelling of welding* (2nd ed.). The Institute of Materials.

[47] Davis, S. H. (2001). *Theory of solidification*. Cambridge University Press.

[48] Kurz, W. (2001). Solidification microstructure-processing maps: Theory and application. *Advanced Engineering Materials, 3*(7), 443–452. [CrossRef]

[49] Dong, H., & Lee, P. D. (2005). Simulation of the columnar-to-equiaxed transition in directionally solidified Al–Cu alloys. *Acta Materialia, 53*(3), 659–668. [CrossRef]

[50] Hunt, J. D. (1984). Steady state columnar and equiaxed growth of dendrites and eutectic. *Materials Science and Engineering, 65*(1), 75–83. [CrossRef]

[51] Kurz, W., Bezençon, C., & Gäumann, M. (2001). Columnar to equiaxed transition in solidification processing. *Science and technology of advanced materials, 2*(1), 185-191. [CrossRef]

[52] Jia, Y., Chen, X., Le, Q., & Xin, Y. (2024). The role of different electromagnetic fields in magnesium alloys direct-chill casting: Numerical simulation and experimental investigation. *Journal of Magnesium and Alloys, 12*(12), 5005–5023. [CrossRef]

[53] Wu, M., & Ludwig, A. (2007). Using a three-phase deterministic model for the columnar-to-equiaxed transition. *Metallurgical and Materials Transactions A, 38*(7), 1465–1475. [CrossRef]

[54] Tiwari, S., & Ghosh, S. (2025). Orientation selection in alloy dendritic evolution during melt-pool solidification. *Computational Materials Science, 249*, 113664. [CrossRef]

[55] Wang, W., Liu, W., Yang, X., Xu, R., & Dai, Q. (2022). Multi-scale simulation of columnar-to-equiaxed transition during laser selective melting of rare earth magnesium alloy. *Journal of Materials Science & Technology, 119*, 11–24. [CrossRef]

[56] He, Y., Zhong, M., Jones, N., Beuth, J., & Webler, B. (2021). The columnar-to-equiaxed transition in melt pools during laser powder bed fusion of M2 steel. *Metallurgical and Materials Transactions A, 52*(9), 4206–4221. [CrossRef]

[57] Chen, C., Wang, J., Liao, H., Ren, Z., & Yin, S. (2020). Laser additive manufacturing of single-crystal superalloy component: from solidification mechanism to grain structure control. In *Laser*

Cladding of Metals (pp. 137-159). Cham: Springer International Publishing. [CrossRef]

[58] Gäumann, M., Bezençon, C., Canalis, P., & Kurz, W. (2001). Single-crystal laser deposition of superalloys: Processing–microstructure maps. *Acta Materialia, 49*(6), 1051–1062. [CrossRef]

[59] Huang, Z., Zhai, Z., Lin, W., Chang, H., Wu, Y., Yang, R., & Zhang, Z. (2022). On the orientation dependent microstructure and mechanical behavior of Hastelloy X superalloy fabricated by laser powder bed fusion. *Materials Science and Engineering: A, 844*, 143208. [CrossRef]

[60] Dragnevski, K., Mullis, A. M., Walker, D. J., & Cochrane, R. F. (2002). Mechanical deformation of dendrites by fluid flow during the solidification of undercooled melts. *Acta materialia, 50*(14), 3743-3755. [CrossRef]

[61] Serrano-Munoz, I., Mishurova, T., Thiede, T., Sprengel, M., Kromm, A., Nadammal, N., ... & Bruno, G. (2020). The residual stress in as-built Laser Powder Bed Fusion IN718 alloy as a consequence of the scanning strategy induced microstructure. *Scientific reports, 10*(1), 14645. [CrossRef]

[62] Li, Z., Lin, X., Sui, S., Zhao, X., Yao, B., Zhong, C., Gasser, A., & Tan, H. (2025). Single-crystal structure formation in laser directed energy deposited Inconel 718 through process parameter optimization and substrate orientation tuning. *Journal of Materials Processing Technology, 335*, 118673. [CrossRef]

[63] Ramsperger, M., & Körner, C. (2016, August). Selective Electron Beam Melting of the Single Crystalline Nickel-Base Superalloy CMSX-4®: From Columnar Grains to a Single Crystal. In *Superalloys 2016: Proceedings of the 13th Intenational Symposium of Superalloys* (pp. 341-349). Hoboken, NJ, USA: John Wiley & Sons, Inc.. [CrossRef]

[64] Li, Z., Li, H., Yin, J., Li, Y., Nie, Z., Li, X., ... & Hao, L. (2022). A review of spatter in laser powder bed fusion additive manufacturing: In situ detection, generation, effects, and countermeasures. *Micromachines, 13*(8), 1366. [CrossRef]

[65] Priarone, P. C., Lunetto, V., Atzeni, E., & Salmi, A. (2018). Laser powder bed fusion (L-PBF) additive manufacturing: On the correlation between design choices and process sustainability. *Procedia CIRP, 78*, 85–90. [CrossRef]

[66] Gokcekaya, O., Ishimoto, T., Hibino, S., Yasutomi, J., Narushima, T., & Nakano, T. (2021). Unique crystallographic texture formation in Inconel 718 by laser powder bed fusion and its effect on mechanical anisotropy. *Acta Materialia, 212*, 116876. [CrossRef]

[67] Acharya, R., Bansal, R., Gambone, J. J., & Das, S. (2014). A Coupled Thermal, Fluid Flow, and Solidification Model for the Processing of Single-Crystal Alloy CMSX-4 Through Scanning Laser Epitaxy for Turbine Engine Hot-Section Component Repair (Part I). *Metallurgical and Materials Transactions B, 45*(6), 2247–2261. [CrossRef]

[68] Tao, S., Gao, R., Peng, H., Guo, H., & Chen, B. (2022). High-reliability repair of single-crystal Ni-base superalloy by selective electron beam melting. *Materials & Design, 224*, 111421. [CrossRef]

[69] Kumar, B., Sahu, S., Srinivasan, D., & Jaya, B. N. (2023). Influence of heat input on solidification cracking in additively manufactured CM247LC Ni-based superalloy. *Metallurgical and Materials Transactions A, 54*(6), 2394–2409. [CrossRef]

[70] Yu, Y., Zhang, Z., Xiao, C., Chen, H., Lu, C., & Ma, J. (2024). Investigation of the microstructure and physical properties of TaSi2 sintered at high temperature and high pressure. *Journal of Materials Research and Technology, 29*, 3108–3116. [CrossRef]

[71] Tang, Y. T., Panwisawas, C., Ghoussoub, J. N., Gong, Y., Clark, J. W. G., Németh, A. A. N., McCartney, D. G., & Reed, R. C. (2021). Alloys-by-design: Application to new superalloys for additive manufacturing. *Acta Materialia, 202*, 417–436. [CrossRef]

[72] Wang, D., Liu, Z., Deng, G., Zhou, X., Li, S., Wang, H., Yang, Y., & Han, C. (2024). A laser powder bed fusion–based methodology for repairing damaged nickel-based turbine blades: Investigation of interfacial characteristics and hot isostatic pressing treatment. *Materials Characterization, 212*, 113948. [CrossRef]

[73] Abdelwahed, M., Puchades, J. R. B., Griñán, L. P., Ceniceros, M. M., Rovatti, L., Ishola, R. M., & Vedani, M. (2023). Cracking mechanisms and effect of extensive preheating in CM247LC and IN713LC Ni-base superalloy processed by Laser Powder Bed Fusion. *Materials Today Communications, 37*, 107644. [CrossRef]

[74] Li, L., Dong, T., Jiang, F., Ru, Y., Guo, C., Diao, M., & Song, H. (2024). A novel method enhanced mechanical properties of a selective laser melted Mar-M247 superalloy by progressive remelting. *Journal of Materials Research and Technology, 33*, 4968–4980. [CrossRef]

[75] Jena, A., Atabay, S. E., Gontcharov, A., Lowden, P., & Brochu, M. (2021). Laser powder bed fusion of a new high gamma prime Ni-based superalloy with improved weldability. *Materials & Design, 208*, 109895. [CrossRef]

[76] Singh, R., Gupta, A., Tripathi, O., Srivastava, S., Singh, B., Awasthi, A., ... & Saxena, K. K. (2020). Powder bed fusion process in additive manufacturing: An overview. *Materials Today: Proceedings, 26*, 3058-3070. [CrossRef]

[77] Fernandez-Zelaia, P., Kirka, M. M., Rossy, A. M., Lee, Y., & Dryepondt, S. N. (2021). Nickel-based superalloy single crystals fabricated via electron beam melting. *Acta Materialia, 216*, 117133. [CrossRef]

[78] Hamdi, H., Sadatabhari, S., Tajik, A., Hanzaki, A. Z., Hatamiyan, A., & Abedi, H. R. (2025). From melt pool to performance: A review of microstructural engineering in the additive manufacturing of nickel-based superalloys. *Results in Engineering, 28*, 107402. [CrossRef]

[79] Ramsperger, M., & Eichler, S. (2023). Electron Beam Based Additive Manufacturing of Alloy 247 for Turbine Engine Application: From Research towards Industrialization. *Metallurgical and Materials Transactions A, 54*(5), 1730–1743. [CrossRef]

[80] Chauvet, E., Tassin, C., Blandin, J. J., Dendievel, R., & Martin, G. (2018). Producing Ni-base superalloys single crystal by selective electron beam melting. *Scripta Materialia, 152*, 15-19. [CrossRef]

[81] Li, Y., Yu, Y. F., Wang, Z. B., Liang, X. Y., Kan, W. B., & Lin, F. (2022). Additive manufacturing of nickel-based superalloy single crystals with IN-738 alloy. *Acta Metallurgica Sinica (English Letters), 35*(3), 369-374. [CrossRef]

[82] Liu, G., Du, D., Wang, K., Pu, Z., & Chang, B. (2021). Epitaxial growth behavior and stray grains formation mechanism during laser surface re-melting of directionally solidified nickel-based superalloys. *Journal of Alloys and Compounds, 853*, 157325. [CrossRef]

[83] Pistor, J., Breuning, C., & Körner, C. (2021). A single crystal process window for electron beam powder bed fusion additive manufacturing of a cmsx-4 type ni-based superalloy. *Materials, 14*(14), 3785. [CrossRef]

[84] Velu, R., Kumar, S. A., & Whenish, R. (2023). Processing challenges in additively manufactured single crystal alloys: a process–structure–property relationship approach. In *Advances in Additive Manufacturing* (pp. 253-264). Elsevier. [CrossRef]

[85] Bäreis, J., Wahlmann, B., & Körner, C. (2025). Single crystal twisting in additive manufacturing. *Progress in Additive Manufacturing, 10*(10), 8795–8801. [CrossRef]

[86] Li, Y., Liang, X., Peng, G., & Lin, F. (2022). Effect of heat treatments on the microstructure and mechanical properties of IN738LC prepared by electron beam powder bed fusion. *Journal of Alloys and Compounds, 918*, 165807. [CrossRef]

[87] Cao, Y., Bai, P., Liu, F., & Hou, X. (2020). Grain growth in IN718 superalloy fabricated by laser additive manufacturing. *Materials Science and Technology, 36*(6), 765-769. [CrossRef]

[88] Zhao, Y., Ma, T., Gao, Z., Feng, Y., Li, C., Guo, Q., ... & Liu, Y. (2023). Significant reduction of grain size and texture intensity in laser powder bed fusion fabricated nickel-based superalloy by increasing constitutional supercooling. *Composites Part B: Engineering, 266*, 111040. [CrossRef]

[89] Buchbender, I., Hoff, C., Hermsdorf, J., Wesling, V., & Kaierle, S. (2020). Single-crystal height extension by Laser Metal Deposition of CMSX-4. *Procedia Cirp, 94*, 304-309. [CrossRef]

[90] Rottwinkel, B. A. P. I. A., Pereira, A., Alfred, I., Noelke, C., Wesling, V., & Kaierle, S. (2017). Turbine blade tip single crystalline clad deposition with applied remelting passes for well oriented volume extension. *Journal of Laser Applications, 29*(2). [CrossRef]

[91] Vilar, R., & Almeida, A. (2015). Repair and manufacturing of single crystal Ni-based superalloys components by laser powder deposition—A review. *Journal of Laser Applications, 27*(S1), S17004. [CrossRef]

[92] Zhang, P., Zhou, X., Zhang, W., Zhang, T., Ding, G., & Cheng, X. (2022). Effects of melt-pool geometry on the oriented to misoriented transition in directed energy deposition of a single-crystal superalloy. *Additive Manufacturing, 60*, 103253. [CrossRef]

[93] Ünal-Saewe, T., Gahn, L., Kittel, J., Gasser, A., & Schleifenbaum, J. H. (2020). Process development for tip repair of complex shaped turbine blades with IN718. *Procedia Manufacturing, 47*, 1050–1057. [CrossRef]

[94] Bhure, S., Nalajala, D., & Choudhury, A. (2024). Toward DS/SX Ni-Based Superalloy Components Using L-DED: A Multi-scale Modeling and Experimental Approach. *Transactions of the Indian Institute of Metals, 77*(10), 2945–2952. [CrossRef]

[95] Bhure, S., Nalajala, D., & Choudhury, A. (2025). Single-crystalline Ni-based superalloy builds using laser-directed energy deposition (L-DED): A multi-scale modeling and experimental approach. *Acta Materialia, 286*, 120703. [CrossRef]

[96] Wilson, J. M., Piya, C., Shin, Y. C., Zhao, F., & Ramani, K. (2014). Remanufacturing of turbine blades by laser direct deposition with its energy and environmental impact analysis. *Journal of Cleaner Production, 80*, 170–178. [CrossRef]

[97] Mallikarjuna, B., & Reutzel, E. W. (2022). Reclamation of intermetallic titanium aluminide aero-engine components using directed energy deposition technology. *Manufacturing Review, 9*, 27. [CrossRef]

[98] Hooper, P. A. (2018). Melt pool temperature and cooling rates in laser powder bed fusion. *Additive Manufacturing, 22*, 548-559. [CrossRef]

[99] del Bosque, A., Fernández-Arias, P., & Vergara, D. (2025). Advances in the additive manufacturing of superalloys. *Journal of Manufacturing and Materials Processing, 9*(7), 215. [CrossRef]

[100] Wang, Z., Liu, F., Gao, S., Li, Q., & Chen, K. (2026). Turn Nonweldable Ni-Superalloys Printable and Microstructurally Controllable. *Advanced Materials, 38*(4), e17003. [CrossRef]

[101] Liu, Z., Zhao, D., Wang, P., Yan, M., Yang, C., Chen, Z., Lu, J., & Lu, Z. (2022). Additive manufacturing

of metals: Microstructure evolution and multistage control. *Journal of Materials Science & Technology, 100*, 224–236. [CrossRef]

[102] Griffith, M. L., Ensz, M. T., Puskar, J. D., Robino, C. V., Brooks, J. A., Philliber, J. A., ... & Hofmeister, W. H. (2000). Understanding the microstructure and properties of components fabricated by laser engineered net shaping (LENS). *MRS Online Proceedings Library (OPL), 625*, 9. [CrossRef]

[103] Svetlizky, D., Das, M., Zheng, B., Vyatskikh, A. L., Bose, S., Bandyopadhyay, A., Schoenung, J. M., Lavernia, E. J., & Eliaz, N. (2021). Directed energy deposition (DED) additive manufacturing: Physical characteristics, defects, challenges and applications. *Materials Today, 49*, 271–295. [CrossRef]

[104] Manvatkar, V., De, A., & DebRoy, T. (2014). Heat transfer and material flow during laser assisted multi-layer additive manufacturing. *Journal of Applied Physics, 116*(12), 124905. [CrossRef]

[105] Bermingham, M., StJohn, D., Krynen, J., Tedman-Jones, S., & Dargusch, M. (2019). Promoting the columnar to equiaxed transition and grain refinement of titanium alloys during additive manufacturing. *Acta Materialia, 168*, 261–274. [CrossRef]

[106] Liu, P., Wang, Z., Xiao, Y., Horstemeyer, M. F., Cui, X., & Chen, L. (2019). Insight into the mechanisms of columnar to equiaxed grain transition during metallic additive manufacturing. *Additive Manufacturing, 26*, 22–29. [CrossRef]

[107] Gotterbarm, M. R., Rausch, A. M., & Körner, C. (2020). Fabrication of Single Crystals through a μ-Helix Grain Selection Process during Electron Beam Metal Additive Manufacturing. *Metals, 10*(3), 313. [CrossRef]

[108] Rajurkar, A., & Chinchanikar, S. (2024). Investigation on the effect of laser parameters and hatch patterns on the dimensional accuracy of micro-dimple and micro-channel texture geometries. *International Journal on Interactive Design and Manufacturing, 18*(10), 7021–7038. [CrossRef]

[109] Li, H., Shen, Y., Wu, X., Wang, D., & Yang, Y. (2024). Advances in laser powder bed fusion of tungsten, tungsten alloys, and tungsten-based composites. *Micromachines, 15*(8), 966. [CrossRef]

[110] Zhang, D., Prasad, A., Bermingham, M. J., Todaro, C. J., Benoit, M. J., Patel, M. N., Qiu, D., StJohn, D. H., Qian, M., & Easton, M. A. (2020). Grain refinement of alloys in fusion-based additive manufacturing processes. *Metallurgical and Materials Transactions A, 51*(9), 4341–4359. [CrossRef]

[111] Liu, X., Hu, R., Zou, H., Yang, C., Luo, X., Bai, J., & Ma, R. (2023). Investigation of cracking mechanism and yield strength associated with scanning strategy for an additively manufactured nickel-based superalloy. *Journal of Alloys and Compounds, 938*, 168532. [CrossRef]

[112] Nadammal, N., Mishurova, T., Fritsch, T., Serrano-Munoz, I., Kromm, A., Haberland, C., Portella, P. D., & Bruno, G. (2021). Critical role of scan strategies on the development of microstructure, texture, and residual stresses during laser powder bed fusion additive manufacturing. *Additive Manufacturing, 38*, 101792. [CrossRef]

[113] Chen, Q., Taylor, H., Takezawa, A., Liang, X., Jimenez, X., Wicker, R., & To, A. C. (2021). Island scanning pattern optimization for residual deformation mitigation in laser powder bed fusion via sequential inherent strain method and sensitivity analysis. *Additive Manufacturing, 46*, 102116. [CrossRef]

[114] Holman, D., Boseila, J., & Schleifenbaum, J. H. (2025). New Island Partitioning to Improve Scanning Strategies in Powder Bed Fusion of Metals with Laser Beam. *BHM Berg-Und Hüttenmännische Monatshefte, 170*(3), 140–147. [CrossRef]

[115] Xie, X., Zhang, F., Peng, C., Yan, X., Chao, Q., Li, Y., Li, R., Liu, X., & Fan, G. (2025). Effect of scan strategy and substrate preheating on crack formation in IN738LC Ni-based superalloy during laser powder bed fusion. *Materials Characterization, 221*, 114722. [CrossRef]

[116] Ravichander, B. B., Mamidi, K., Rajendran, V., Farhang, B., Ganesh-Ram, A., Hanumantha, M., Moghaddam, N. S., & Amerinatanzi, A. (2022). Experimental investigation of laser scan strategy on the microstructure and properties of Inconel 718 parts fabricated by laser powder bed fusion. *Materials Characterization, 186*, 111765. [CrossRef]

[117] Wang, J., Zhu, R., Liu, Y., & Zhang, L. (2023). Understanding melt pool characteristics in laser powder bed fusion: An overview of single-and multi-track melt pools for process optimization. *Advanced Powder Materials, 2*(4), 100137. [CrossRef]

[118] Lu, Y., Wu, S., Gan, Y., Huang, T., Yang, C., Junjie, L., & Lin, J. (2015). Study on the microstructure, mechanical property and residual stress of SLM Inconel-718 alloy manufactured by differing island scanning strategy. *Optics & Laser Technology, 75*, 197–206. [CrossRef]

[119] Catchpole-Smith, S., Aboulkhair, N., Parry, L., Tuck, C., Ashcroft, I. A., & Clare, A. (2017). Fractal scan strategies for selective laser melting of 'unweldable' nickel superalloys. *Additive Manufacturing, 15*, 113–122. [CrossRef]

[120] Yang, Z., Koepf, J. A., Markl, M., & Körner, C. (2024). Effect of Scanning Strategies on Grain Structure and Texture of Additively Manufactured Lattice Struts: A Numerical Exploration. *Advanced Engineering Materials, 26*(18), 2400661. [CrossRef]

[121] Gotterbarm, M. R., Seifi, M., Melzer, D., Džugan, J., Salem, A. A., Liu, Z. H., & Koerner, C. (2020). Small scale testing of IN718 single crystals manufactured

by EB-PBF. *Additive Manufacturing, 36*, 101449. [CrossRef]

[122] Thawari, N., Gullipalli, C., & Gupta, T. V. K. (2022). Effect of Laser Spot Diameter on Melt Pool Thermal History During Laser Cladding on Inconel 718 Coatings. In *Recent Trends in Design, Materials and Manufacturing: Selected Proceedings of ICRADMM 2020* (pp. 65-73). Springer Nature Singapore. [CrossRef]

[123] Lu, X., Chiumenti, M., Cervera, M., Li, J., Lin, X., Ma, L., Zhang, G., & Liang, E. (2021). Substrate design to minimize residual stresses in Directed Energy Deposition AM processes. *Materials & Design, 202*, 109525. [CrossRef]

[124] Wang, Y., & Shi, J. (2020). Developing very strong texture in a nickel-based superalloy by selective laser melting with an ultra-high power and flat-top laser beam. *Materials Characterization, 165*, 110372. [CrossRef]

[125] Keshavarzkermani, A., Marzbanrad, E., Esmaeilizadeh, R., Mahmoodkhani, Y., Ali, U., Enrique, P. D., Zhou, N. Y., Bonakdar, A., & Toyserkani, E. (2019). An investigation into the effect of process parameters on melt pool geometry, cell spacing, and grain refinement during laser powder bed fusion. *Optics & Laser Technology, 116*, 83–91. [CrossRef]

[126] Bakhtari, A. R., Sezer, H. K., Canyurt, O. E., Eren, O., Shah, M., & Marimuthu, S. (2024). A Review on Laser Beam Shaping Application in Laser-Powder Bed Fusion. *Advanced Engineering Materials, 26*(14), 2302013. [CrossRef]

[127] Li, E., Shen, H., Wang, L., Wang, G., & Zhou, Z. (2023). Laser shape variation influence on melt pool dynamics and solidification microstructure in laser powder bed fusion. *Additive Manufacturing Letters, 6*, 100141. [CrossRef]

[128] Stoll, T., Prudlik, R., Birg, M., & Wudy, K. (2025). Influence of different beam shapes on melt pool geometry of single melt tracks on in718. *Progress in Additive Manufacturing, 10*(4), 2675–2690. [CrossRef]

[129] Jang, H. S., Kim, S. H., Park, G.-W., Jeon, J. B., Kim, D., Choi, Y. S., & Shin, S. (2025). Effects of laser-beam diameter on melt pool characteristics and grain formation in Fe-3.4 wt% Si alloy made by powder bed fusion. *Journal of Materials Research and Technology, 36*, 2938–2950. [CrossRef]

[130] Yang, Z., Li, X., Chang, J., Wu, Z., Yang, Y., & Zhang, Z. (2025). On the stray grains in single-crystal Ni-based superalloy by additive manufacturing: Formation mechanism and elimination strategy. *Journal of Materials Research and Technology, 36*, 7125–7134. [CrossRef]

[131] Guo, C., Li, G., Li, S., Hu, X., Lu, H., Li, X., Xu, Z., Chen, Y., Li, Q., & Lu, J. (2023). Additive manufacturing of Ni-based superalloys: Residual stress, mechanisms of crack formation and strategies for crack inhibition. *Nano Materials Science, 5*(1), 53–77. [CrossRef]

[132] Aucott, L., Huang, D., Dong, H. B., Wen, S. W., Marsden, J., Rack, A., & Cocks, A. C. F. (2018). A three-stage mechanistic model for solidification cracking during welding of steel. *Metallurgical and Materials Transactions A, 49*(5), 1674-1682. [CrossRef]

[133] Chen, M., Hua, L., Hu, Z., Dong, K., & Qin, X. (2025). Cracking and suppression mechanisms of directed energy deposited IN738 superalloy revealed by microstructural characterization, in-situ thermal monitoring, and numerical simulations. *Journal of Alloys and Compounds, 1020*, 179446. [CrossRef]

[134] Wei, Q., Xie, Y., Teng, Q., Shen, M., Sun, S., & Cai, C. (2022). Crack types, mechanisms, and suppression methods during high-energy beam additive manufacturing of nickel-based superalloys: A review. *Chinese Journal of Mechanical Engineering: Additive Manufacturing Frontiers, 1*(4), 100055. [CrossRef]

[135] Zhang, X., Mu, Y., Lu, N., Li, Q., Chen, S., Zhou, Y., Sun, X., Liang, J., & Li, J. (2024). Effect of solid solution elements on cracking susceptibility of Ni-based superalloys during additive manufacturing. *Journal of Materials Science & Technology, 190*, 218–228. [CrossRef]

[136] Rakoczy, Ł., Grudzień-Rakoczy, M., Rutkowski, B., Cygan, R., & Zielińska-Lipiec, A. (2024). The role of the microstructural changes during induction preheating on the HAZ liquation cracking susceptibility of Ni-based superalloy. *Journal of Materials Science, 59*(2), 631–649. [CrossRef]

[137] Shahwaz, M., Nath, P., & Sen, I. (2025). Recent advances in additive manufacturing technologies for Ni-Based Inconel superalloys–A comprehensive review. *Journal of Alloys and Compounds, 1010*, 177654. [CrossRef]

[138] Griffiths, S., Tabasi, H. G., Ivas, T., Maeder, X., De Luca, A., Zweiacker, K., Wróbel, R., Jhabvala, J., Logé, R., & Leinenbach, C. (2020). Combining alloy and process modification for micro-crack mitigation in an additively manufactured Ni-base superalloy. *Additive Manufacturing, 36*, 101443. [CrossRef]

[139] Gerstgrasser, M., Cloots, M., Stirnimann, J., & Wegener, K. (2021). Residual stress reduction of LPBF-processed CM247LC samples via multi laser beam strategies. *The International Journal of Advanced Manufacturing Technology, 117*(7), 2093–2103. [CrossRef]

[140] Wei, C., Zhu, D., Xia, Z., Zhao, Z., Zhu, T., Tang, H., Wang, C., Yang, J., Shen, X., & Tang, J. (2025). Synergize dual-laser-induced in-situ remelting and high-temperature heat treatment to achieve extraordinary strength and toughness of additively manufactured tungsten heavy alloy.

Materials Science and Engineering: A, 926, 148829. [CrossRef]

[141] Alkunte, S., Gupta, M., Shingare, K., More, N., Mali, A., Ingle, N., ... & Fidan, I. (2025). Porosity in additive manufacturing: influence on mechanical, thermal, and electrical properties—a review. *The International Journal of Advanced Manufacturing Technology, 140*(5), 2397-2421. [CrossRef]

[142] Brennan, M. C., Keist, J. S., & Palmer, T. A. (2021). Defects in Metal Additive Manufacturing Processes. *Journal of Materials Engineering and Performance, 30*(7), 4808–4818. [CrossRef]

[143] Liu, D., Pan, Y., Hou, H., & Zhao, Y. (2026). Pore evolution and porosity mitigation in laser powder bed fusion of Ni-Cr-Fe based superalloy. *International Journal of Heat and Mass Transfer, 255*, 127781. [CrossRef]

[144] Rabin, B., Smolik, G., & Korth, G. (1990). Characterization of entrapped gases in rapidly solidified powders. *Materials Science and Engineering: A, 124*(1), 1–7. [CrossRef]

[145] Sun, C., Li, W., Li, C., Sun, R., Liu, G., & Li, X. (2025). Study on microstructure and fatigue properties of laser powder bed fusion nickel-based superalloy with heat treatment. *Additive Manufacturing Frontiers, 4*(2), 200217. [CrossRef]

[146] Guo, L., Liu, H., Wang, H., Wei, Q., Xiao, Y., Tang, Z., Wu, Y., & Wang, H. (2023). Identifying the keyhole stability and pore formation mechanisms in laser powder bed fusion additive manufacturing. *Journal of Materials Processing Technology, 321*, 118153. [CrossRef]

[147] King, W. E., Barth, H. D., Castillo, V. M., Gallegos, G. F., Gibbs, J. W., Hahn, D. E., Kamath, C., & Rubenchik, A. M. (2014). Observation of keyhole-mode laser melting in laser powder-bed fusion additive manufacturing. *Journal of Materials Processing Technology, 214*(12), 2915–2925. [CrossRef]

[148] Wang, H., & Zou, Y. (2019). Microscale interaction between laser and metal powder in powder-bed additive manufacturing: Conduction mode versus keyhole mode. *International Journal of Heat and Mass Transfer, 142*, 118473. [CrossRef]

[149] Sanaei, N., Fatemi, A., & Phan, N. (2019). Defect characteristics and analysis of their variability in metal L-PBF additive manufacturing. *Materials & Design, 182*, 108091. [CrossRef]

[150] Ayeni, T., Karimi, P., Keshavarz, M. K., Sadeghi, E., Habibnejad-korayem, M., & Vlasea, M. (2025). Comprehensive pore defect analysis for electron beam-powder bed fusion of Ti48Al2Cr2Nb. *Advances in Industrial and Manufacturing Engineering, 10*, 100170. [CrossRef]

[151] Han, Q., Mertens, R., Montero-Sistiaga, M. L., Yang, S., Setchi, R., Vanmeensel, K., ... & Fan, H. (2018). Laser powder bed fusion of Hastelloy X: Effects of hot isostatic pressing and the hot cracking mechanism. *Materials Science and Engineering: A, 732*, 228-239. [CrossRef]

[152] Sanchez, S., Smith, P., Xu, Z., Gaspard, G., Hyde, C. J., Wits, W. W., Ashcroft, I. A., Chen, H., & Clare, A. T. (2021). Powder bed fusion of nickel-based superalloys: A review. *International Journal of Machine Tools and Manufacture, 165*, 103729. [CrossRef]

[153] Tammas-Williams, S., Withers, P. J., Todd, I., & Prangnell, P. B. (2016). The effectiveness of hot isostatic pressing for closing porosity in titanium parts manufactured by selective electron beam melting. *Metallurgical and Materials Transactions A, 47*(5), 1939-1946. [CrossRef]

[154] Baturynska, I. (2018). Statistical analysis of dimensional accuracy in additive manufacturing considering STL model properties. *The International Journal of Advanced Manufacturing Technology, 97*(5), 2835–2849. [CrossRef]

[155] Mostafaei, A., Ghiaasiaan, R., Ho, I. T., Strayer, S., Chang, K. C., Shamsaei, N., ... & To, A. C. (2023). Additive manufacturing of nickel-based superalloys: A state-of-the-art review on process-structure-defect-property relationship. *Progress in Materials Science, 136*, 101108. [CrossRef]

[156] Du, Z., Li, H., You, R., & Huang, Y. (2023). Effects of thermal barrier coating thickness and surface roughness on cooling performance sensitivity of a turbine blade. *Case Studies in Thermal Engineering, 52*, 103727. [CrossRef]

[157] Jamshidinia, M., & Kovacevic, R. (2015). The influence of heat accumulation on the surface roughness in powder-bed additive manufacturing. *Surface Topography: Metrology and Properties, 3*(1), 014003. [CrossRef]

[158] Abruzzo, M., Macoretta, G., Monelli, B., & Romoli, L. (2025). Unveiling surface roughness in inconel 718 fabricated by LPBF using high-productivity parameters: A dual method exploration. *Precision Engineering, 94*, 783–794. [CrossRef]

[159] Ali, U., Fayazfar, H., Ahmed, F., & Toyserkani, E. (2020). Internal surface roughness enhancement of parts made by laser powder-bed fusion additive manufacturing. *Vacuum, 177*, 109314. [CrossRef]

[160] Nagalingam, A. P., & Yeo, S. H. (2020). Surface finishing of additively manufactured inconel 625 complex internal channels: A case study using a multi-jet hydrodynamic approach. *Additive Manufacturing, 36*, 101428. [CrossRef]

[161] Syrlybayev, D., Seisekulova, A., Talamona, D., & Perveen, A. (2022). The Post-Processing of Additive Manufactured Polymeric and Metallic Parts. *Journal of Manufacturing and Materials Processing, 6*(5), 116. [CrossRef]

[162] Wu, D., Feng, J., Wang, Y., Wang, Z., Wu, M., & Han, Q. (2025). Laser powder bed fusion of

a novel crack-free γ' phase-strengthened Ni-based alloy. *Materials*, *18*(2), 237. [CrossRef]

Anhui Xiong A PhD student at Nanjing University of Science and Technology, China. His research focuses on the additive manufacturing of high-temperature superalloys, with an emphasis on elucidating critical process-structure-property relationships to enhance material performance in extreme service environments. (Email: ahxiong@njust.edu.cn)

Xianghui Wang Postdoctoral Researcher in the School of Materials Science and Engineering, Nanjing University of Science and Technology. His research focuses on microstructure control of TiAl alloys via electron beam additive manufacturing and solid-state phase transformations. (Email: wangxh@njust.edu.cn)

Pan Ying Graduated from Central South University with a bachelor's degree in 2012, and received his PhD degree in materials science from Yanshan University in 2020. Currently, he works as an associate professor in State Key Laboratory of Advanced Casting Technologies, Nanjing University of Science and Technology. His research focuses on the thermal protection materials and structures. (Email: yingpan@njust.edu.cn)

Chen Chang A PhD student at Nanjing University of Science and Technology, China. He earned his BS degree from Nanjing Institute of Technology and enrolled in the School of Materials Science and Engineering at Nanjing University of Science and Technology in 2024. His research is mainly focused on electron beam precision forming. (Email: Changchen@njust.edu.cn)

Ze Li A doctoral candidate at Nanjing University of Science and Technology, China. He earned his bachelor's and master's degrees from North University of China. In 2024, he began his doctoral studies at Nanjing University of Science and Technology. His research is mainly focused on the additive manufacturing of metallic and intermetallic materials. (Email: nuclize@163.com)

Dong Zheng An undergraduate student of the Dingxin Class of the 2022 grade at Nanjing University of Science and Technology, China. (Email: 3157781153@qq.com)

Shuang Shi Associate professor at Nanjing University of Science and Technology. He is dedicated to the development of high-performance alloy materials, the preparation of ultra-pure materials. He presided over the Advanced Materials-National Science and Technology Major Project, the National Natural Science Foundation of China and other projects. He has published over 50 scientific papers, and awarded 4 provincial/ministerial-level scientific and technological awards. (Email: shishuang@njust.edu.cn)

Yang Chen A professor at Nanjing University of Science and Technology, China. He earned his BS degree from the Georgia Institute of Technology and his MS degree from the University of Michigan, Ann Arbor. After obtaining his PhD degree in materials science and engineering from the University of California, Los Angeles, he became a research scientist at Nanjing University of Science and Technology in 2020. His research is mainly focused on advanced manufacturing and characterization of metallic and intermetallic materials. (Email: yang.chen@njust.edu.cn)